Simulating biosignatures from pre-oxygen photosynthesising life on TRAPPIST-1e

Jake K. Eager-Nash,[1,2]★ Stuart J. Daines,[3] James W. McDermott,[1,7] Peter Andrews,[1] Lucy A. Grain,[1] James Bishop,[1] Aaron A. Rogers,[1] Jack W. G. Smith,[1] Chadiga Khalek,[4] Thomas J. Boxer,[4] Mei Ting Mak,[1] Robert J. Ridgway,[1] Eric Hébrard,[1] F. Hugo Lambert,[5] Timothy M. Lenton,[6] and Nathan J. Mayne[1]

[1]*Department of Physics and Astronomy, University of Exeter, Exeter, UK*
[2]*School of Earth and Ocean Sciences, University of Victoria, Victoria, BC, Canada*
[3]*University of Exeter, Exeter, UK*
[4]*Natural Sciences, University of Exeter, Exeter, UK*
[5]*Department of Mathematics and Statistics, University of Exeter, Exeter, UK*
[6]*Global Systems Institute, University of Exeter, Exeter, UK*
[7]*The Natural History Museum, London, UK*

ABSTRACT

In order to assess observational evidence for potential atmospheric biosignatures on exoplanets, it will be essential to test whether spectral fingerprints from multiple gases can be explained by abiotic or biotic-only processes. Here, we develop and apply a coupled 1D atmosphere-ocean-ecosystem model to understand how primitive biospheres, which exploit abiotic sources of H_2, CO and O_2, could influence the atmospheric composition of rocky terrestrial exoplanets. We apply this to the Earth at 3.8 Ga and to TRAPPIST-1e. We focus on metabolisms that evolved before the evolution of oxygenic photosynthesis, which consume H_2 and CO and produce potentially detectable levels of CH_4. O_2-consuming metabolisms are also considered for TRAPPIST-1e, as abiotic O_2 production is predicted on M-dwarf orbiting planets. We show that these biospheres can lead to high levels of surface O_2 (approximately 1–5 %) as a result of CO consumption, which could allow high O_2 scenarios, by removing the main loss mechanisms of atomic oxygen. Increasing stratospheric temperatures, which increases atmospheric OH can reduce the likelihood of such a state forming. O_2-consuming metabolisms could also lower O_2 levels to around 10 ppm and support a productive biosphere at low reductant inputs. Using predicted transmission spectral features from CH_4, CO, O_2/O_3 and CO_2 across the hypothesis space for tectonic reductant input, we show that biotically-produced CH_4 may only be detectable at high reductant inputs. CO is also likely to be a dominant feature in transmission spectra for planets orbiting M-dwarfs, which could reduce the confidence in any potential biosignature observations linked to these biospheres.

Key words: Astrobiology – planets and satellites: Atmosphere – Exoplanets – planets and satellites: terrestrial planets

1 INTRODUCTION

Planets orbiting M-dwarfs provide the most realistic opportunity for detecting biosignatures in the near future, through JWST and other telescopes in development, such as the European Extremely Large Telescope (ELT). JWST has already been used to determine that TRAPPIST-1b+c are unlikely to have thick atmospheres (Greene et al. 2023; Zieba et al. 2023), but could have surface pressures of up to 10 bar (Ih et al. 2023; Lincowski et al. 2023). In order to detect potential life on these planets, which are orbiting very different host stars to our Sun, it is important to not only study the potential abiotic atmospheres of these planets, but also the potential relationship between life, the atmosphere and the host star (Catling et al. 2018).

Life on other planets may most likely resemble life on the early Earth, rather than the modern day. Life was thought to have emerged during the early Archean, by 3.7 Ga at the latest (Rosing 1999), with potential for life to have emerged much earlier (Knoll & Nowak 2017). Since then, life on Earth has diversified hugely, undergoing major evolutionary revolutions including the evolution of oxygenic photosynthesis and multi-cellular eukaryotes (Lenton & Watson 2011). The number of evolutionary steps, as well as their potential difficulty, which are required to get to higher levels of complexity means that many planets may be limited to more primitive life (Watson 2008). Simple microbial biospheres similar to those that existed during the Archean could be the most common.

The detection of primitive biospheres via their effect on CH_4 and CO has been considered for planets (around Sun-like stars), with ecosystems driven by H_2 and CO consumption, leading to atmospheres with a low CO:CH_4 ratio (Sauterey et al. 2020; Thompson

★ E-mail: jeagernash@uvic.ca (JKE-N)

et al. 2022). Krissansen-Totton et al. (2018a) predicts that biospheres could produce a detectable disequilibrium with an atmosphere composed of CO_2 and CH_4 in the absence of CO. This may be the most likely source of biosignature detection with current instrumentation (Krissansen-Totton et al. 2018b). A potential additional challenge for the unambiguous identification of biosignatures specific to planets around M-dwarf stars is the accumulation of abiotic CO and possibly O_2. This results from a higher photolysis of CO_2 by a higher FUV flux from the M-dwarf spectrum, combined with a lower rate of recombination of these species due to a lower abundance of OH resulting from the lower NUV flux emitted by M-dwarfs (Harman et al. 2015). Schwieterman et al. (2019) finds that high levels of CO could accumulate on inhabited M–dwarf orbiting planets. Using General circulation models (GCMs) and photochemical models, Fauchez et al. (2019) found that clouds and especially hazes could play an important role in blocking the observations of Archean-like atmospheres in large regions of JWST transmission spectra, however CO_2 features are likely to be readily observable on such planets.

A fundamental challenge to identifying a biosignature from atmospheric concentrations of CH_4, CO and O_2 is that all of these gases have both abiotic and biological sources and sinks, and may participate in biogeochemical cycles through the atmosphere-ocean-surface system. Their concentrations are therefore controlled by the combination of regulatory feedbacks generated by a combination of abiotic and hypothetical biological processes. As argued by Catling et al. (2018), a consistent approach then requires populating a hypothesis space with predictions from exo-Earth system models, applying observational constraints and making full use of available context. This type of model has been applied to the early Earth around the early Sun (Kharecha et al. 2005; Sauterey et al. 2020), however there has yet to be an ecosystem model focusing on the implications of M-dwarfs spectra.

Here, we use a newly developed coupled atmosphere-ocean-ecosystem model to show that a H_2 and CO consuming biosphere, which produces CH_4 as a byproduct, leads to an atmosphere with detectable levels of CO_2 and CH_4, but also large signals of CO for a TRAPPIST-1e analogue. We review the abiotic and ecosystem processes we consider in Sections 2 and 3. In Section 4, we outline the model components used here, with results from the coupled model and subsequent transmission spectra shown in Section 5. In Section 6 we discuss the implications of large CO features in our biotic configuration that can lead to the ambiguous detection of a potential biosphere.

2 ABIOTIC BACKGROUND ASSUMPTIONS AND PROCESSES

We consider a terrestrial planet in the habitable zone of an M-dwarf star, with an Earth-like atmosphere dominated by N_2 and CO_2, with liquid water, noting that this may imply an atypical evolutionary history given the star's extended pre-main sequence phase (Luger & Barnes 2015). This most likely also requires a functioning recycling of the lithosphere of some kind, in order to cycle CO_2 and generate a silicate weathering feedback.

The atmosphere's total hydrogen content will then be controlled by redox balance, i.e. the balance between net surface reductant input and hydrogen escape, and atmospheric composition by the combination of photochemistry and surface processes.

Outgassing at the planetary surface is uncertain. Modern Earth plate tectonics allow for the for efficient cycling of volatiles, which is thought to be important for habitability by controlling CO_2 over

geological time scales (Walker et al. 1981). However, the tectonic history of the Earth remains uncertain (e.g. Palin & Santosh 2021; Lourenço & Rozel 2023) and modern plate tectonics may only have evolved as late as 0.85 Ga (Korenaga 2013). During the Archean, the Earth could have been in a stagnant lid state (Solomatov 1995), where the lithosphere is a single lid and there is little surface motion. In these conditions outgassing rates are thought to be lower (Guimond et al. 2021). Arguments have also been made that plate tectonic could have been preceded by a plutonic squishy lid, a regime that has small strong plates that are separated by warm and weak regions created by plutonism (Lourenço & Rozel 2023), similar to Venus (Harris & Bédard 2014; Davies et al. 2023). Modelling of this regime suggests that outgassing rates could be up to a factor of two higher, assuming an extrusion efficiency of the lithosphere similar to today (Lourenço et al. 2020).

The mix of gases outgassed is affected by the fugacity of the mantle (Kasting et al. 1993; Guimond et al. 2021). A more reduced mantle will outgas more H_2 and CO and less H_2O and CO_2, while a higher mantle fugacity would lead to the opposite (Guimond et al. 2021). A stagnant lid planet may have outgassed significantly less than a planet with plate tectonics (Guimond et al. 2021). Additional tectonically-driven reduced gases may be produced by serpentinization at mid-ocean ridges (potentially a large source of H_2 and possibly CH_4, with H_2 dominating on modern Earth McCollom & Bach 2009).

The atmospheres of planets orbiting M-dwarfs receive a different stellar spectra compared to Earth, which has an effect on climate (Shields et al. 2013; Eager-Nash et al. 2020), as well as the atmospheric composition (Segura et al. 2005; Harman et al. 2015; Rugheimer et al. 2015; Rugheimer & Kaltenegger 2018; Schwieterman et al. 2019; Kozakis et al. 2022). M-dwarfs have a lower proportion of radiation in the ultraviolet range, particularly in the mid and near UV (200-400 nm) (Wunderlich et al. 2020), which is important for photochemistry (Harman et al. 2015). On M-dwarfs, this allows biosignature gases such as CH_4 to be able to be maintained at higher concentration for a given CH_4 outgassing flux due to a lack of OH from water vapour photolysis (Segura et al. 2005; Meadows et al. 2018; Schwieterman et al. 2019).
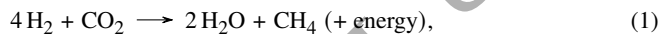
For lifeless planets, it has been found that O_2 may accumulate to significant levels in the atmosphere via the photolysis of CO_2, with a slow catalysed recombination of O and CO, which is caused by a higher ratio of Far UV (FUV, 110–200 nm) to mid and near UV (200–400 nm) compared to the Sun (Tian et al. 2014; Domagal-Goldman et al. 2014; Harman et al. 2015; Ranjan et al. 2023). This is caused by the lower H_2O photolysis resulting from the significantly reduced NUV flux relative to the Sun, which is able to reach close to the surface to photolyse H_2O (Harman et al. 2015). The NUV cross sections for H_2O were found to have been underestimated however, with Ranjan et al. (2020) finding that these increased rates led to higher OH levels, which catalyse the recombination of CO and O to reform CO_2, and removes the possibility of O_2 false positives. NO can be feasibly produced by lightning in the atmosphere and could eradicate the O_2 false positive, by catalysing the recombination of CO and O (Harman et al. 2018). Hu et al. (2020) went on to show that the inclusion of NO_x reservoir species, HO_2NO_2 and N_2O_5, could lead to large abiotic sources of atmospheric O_2. HO_2NO_2 and N_2O_5 act as reservoirs as they are relatively stable and store NO in a form that cannot catalyse CO_2 formation, and would rainout into the oceans. However, it was recently found that this result was due to the model top height being too low (54 km), which leads to erroneously high levels of O production at the model top (Ranjan et al. 2023). Thus, it is now considered unlikely that an O_2 false positive can be produced by CO_2 photolysis (Ranjan et al. 2023).

Although M-dwarfs emit significantly less UV radiation than G-dwarfs, some of these stars can flare regularly (Hawley et al. 2014), which increases UV radiation incident on the planet and significantly impacts atmospheric composition (Chen et al. 2020; Ridgway et al. 2022). For a modern Earth-like atmospheric composition, flaring increases the formation of ozone in the stratosphere, which provides additional protection to the planet's surface from the UV radiation from subsequent flares (Ridgway et al. 2022). Taking a temporally averaged spectrum of a flaring M-dwarf produces a reasonable approximation of the mean chemical composition of an atmosphere experiencing flares (Ridgway et al. 2022).
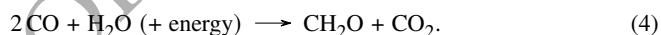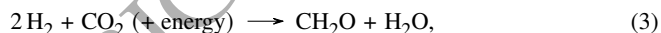
3 ECOSYSTEM PROCESSES

Methanogens are thought to be one of the first organisms to have been present on Earth (Battistuzzi et al. 2004). Methanogens are CH_4-producing microscopic organisms and could have metabolised H_2 from volcanic outgassing. CO–consuming organisms are also thought to have evolved early in Earth's history (Ferry 2006; Lessner et al. 2006; Weiss et al. 2016). These organisms had the potential to impact the composition of the atmosphere by providing a major source of CH_4 (Kharecha et al. 2005), which impacts the climate (Eager-Nash et al. 2023). Models of plausible biospheres on early Earth, which include methanogens, have been used to investigate possible biological productivity and subsequent atmospheric conditions (Kharecha et al. 2005; Ozaki et al. 2018; Sauterey et al. 2020). Kharecha et al. (2005) found that early methanogenic biospheres could have converted the majority of lower atmospheric H_2 to CH_4, producing atmospheres with CH_4 concentrations from 10 to 3,500 ppm. This is controlled by redox balance between reductant input and hydrogen escape, and with cycling of hydrogen through atmospheric CH_4 photolysis and biosphere CH_4 production. We assume that life on other planets may also utilise available H_2 and CO for metabolism, to understand the effect that these biospheres could have on planets that orbit M-dwarfs.

Conceptually, a biosphere could function as summarised schematically in Figure 1, which is the form we take in our model. We now describe a modelling framework that follows similar logic to Kharecha et al. (2005); Ozaki et al. (2018); Sauterey et al. (2020), but is considered in more general terms to apply in an astrobiological context for pre-photosynthetic biospheres exploiting free-energy gradients from available substrates (Nicholson et al. 2022). Organisms use the available H_2 and CO to produce energy (catabolism) via pathways such as:

$$4\,H_2 + CO_2 \longrightarrow 2\,H_2O + CH_4 \text{ (+ energy)}, \tag{1}$$

$$4\,CO + 2\,H_2O \longrightarrow 2\,CO_2 + CH_3COOH \text{ (+ energy)}, \tag{2}$$

where this energy can be used for other metabolic processes such as building biomass (anabolism), represented here as CH_2O:

$$2\,H_2 + CO_2 \text{ (+ energy)} \longrightarrow CH_2O + H_2O, \tag{3}$$

$$2\,CO + H_2O \text{ (+ energy)} \longrightarrow CH_2O + CO_2. \tag{4}$$

The biomass will either descend to the ocean floor once the organism has died and is buried, which contributes a burial of reducing matter

and oxidises the Atmosphere-Ocean system. Alternatively, secondary consumers would evolve that consume and recycle this biomass:

$$2\,CH_2O \longrightarrow CH_3COOH \longrightarrow CH_4 + CO_2. \tag{5}$$

Some fraction of biomass however is inevitably buried, although this percentage is low on Earth with estimates of 0.2% in modern oceans (Berner 1982) and could have been 2% during the past based on studies on anoxic waters (Arthur et al. 1994).

On Earth, anoxygenic photosynthesis evolved relatively early, which provided energy directly to create biomass rather than from catabolism reactions. If this were to occur on other planets for H_2 and CO consuming organisms, we capture this in the model in the simplified form of

$$2\,H_2 + CO_2 + h\nu \longrightarrow CH_2O + H_2O, \tag{6}$$

$$2\,CO + H_2O + h\nu \longrightarrow CH_2O + CO_2. \tag{7}$$
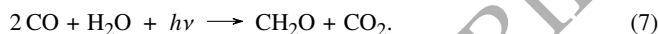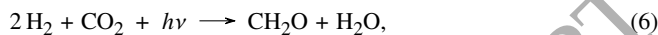
For primary producers, the growth rate is the proportion of total carbon consumed that is fixed into organic matter (CH_2O). This means that the more carbon that can be converted into organic carbon, the faster an organism will grow. Thus, organisms that obtain energy for carbon fixation from the anabolic metabolism of carbon (Equation 3/4) have a low growth rate. Faster growth rates can be achieved when the energy for carbon fixation comes from other sources, such as through photosynthesis (Equation 6), where the growth rate is close to unity. The implication of this for biosignatures is that organisms with higher growth rates produce less biosignature gases (in this case CH_4), meaning efficient recycling and thus a low organic carbon burial rate would be required to produce the largest biosignature possible for this ecosystem.

As abiotic sources of O_2 have been predicted from CO_2 photolysis, its build-up would also provide an energy source for oxic metabolisms, for example by reaction with CH_4 (known on Earth as methanotrophy Kasting et al. 2001):

$$2\,O_2 + CH_4 \longrightarrow 2\,H_2O + CO_2 \text{ (+ energy)}. \tag{8}$$
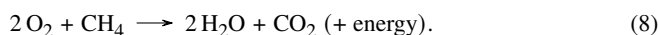
Other pathways would be possible depending on what reducing species are most readily available, such as CO:

$$O_2 + 2\,CO \longrightarrow 2\,CO_2 \text{ (+ energy)}. \tag{9}$$
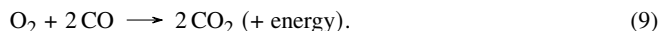
In this work, we assume that the primary productivity of the biosphere is limited by the supply of electron donors. Prior to the evolution of oxygenic photosynthesis, it is thought that primary productivity was limited by electron donor supply (Ward et al. 2019), rather than phosphorus, nitrogen or the availability of other micronutrients. Oxygenic photosynthesis uses H_2O and CO_2 to fix carbon and with both of these species in high abundance, phosphorus and nitrogen therefore limit productivity. Therefore, here (in the absence of oxygenic photosynthesis) we assume that the less abundant electron donors, H_2 and CO, limit productivity, following previous studies (e.g. Kharecha et al. 2005; Ozaki et al. 2018; Sauterey et al. 2020). Other limiting factors could have been important on the early Earth and could be important for exoplanets, with ocean transport playing an key role (Olson et al. 2020; Salazar et al. 2020). Therefore, this work presents upper limits for biosphere productivity for an assumed flux of abiotic H_2 and CO.
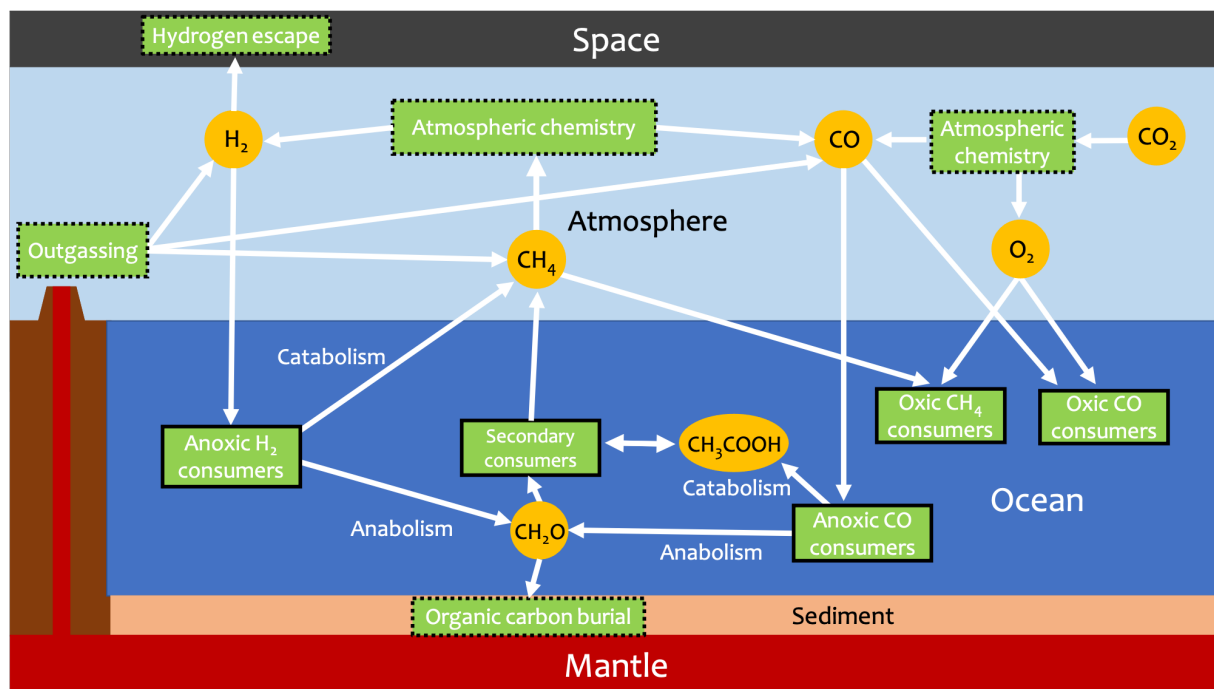
Figure 1. Schematic showing the biosphere reaction pathways and an overview of the interaction with the atmosphere captured in our modelling framework. Green boxes show processes, both biotic (dashed outline) and abiotic (solid outline), circles show reservoirs of species and arrows show fluxes between reservoirs via the different processes. Volcanic outgassing drives biospheric productivity by providing electron donors for primary producers. These are used for either catabolism to produce energy and CH_4 as a waste product, with this energy used for biomass production, which is then either recycled by secondary consumers and eventually converted to CH_4 again or the biomass is buried in the sediments.

4 METHODS

In this work, we use the Platform for Atmosphere, Land, Earth and Ocean (PALEO) modelling framework (Daines & Lenton 2016) to study potential abiotic conditions on planets as well as life resembling that of life on Earth prior to the evolution of oxygenic photosynthesis. PALEO relies on the use of a 1D photochemical atmosphere model coupled to a single box ocean that hosts a biosphere. The model conserves redox balance across the atmosphere ocean system. We do these experiments for Earth around 3.8 Ga, when these ecosystems were thought to be present and for TRAPPIST-1e. TRAPPIST-1e is one of several planets in orbit around TRAPPIST-1 (Gillon et al. 2017), an ultra-cool M-dwarf, with the planets in this system prime targets for atmospheric characterisation. The atmospheric composition and climate solutions for the TRAPPIST-1e simulations are then used to generate synthetic spectra using the Planetary Spectrum Generator (PSG) (Villanueva et al. 2018) to predict the potential detectability of biospheres prior to the evolution of oxygenic photosynthesis on TRAPPIST-1e. The components of this model are now described in more detail.

4.1 Climate solution

The 1D atmosphere includes a radiative-convective model to calculate the climate solution that provides a vertical temperature and humidity profile. This climate state is then used by the photochemical model to calculate chemical rates. For the purpose of this work, these components are not coupled and a single climate solution is used for each planetary configuration, even though atmospheric composition varies.

Radiative transfer is calculated using the Suite Of Commu-

nity RAdiative Transfer codes based on Edwards & Slingo (1996) (SOCRATES) (Manners et al. 2022), with a convective adjustment based on Manabe & Strickler (1964), with a pseudoadiabatic lapse rate. Tropospheric water vapour decreases with temperature (Manabe & Wetherald 1967) with a prescribed surface relative humidity of 70 %. Above the tropopause, the water vapour mixing ratio is fixed at the tropopause value. We obtain a climate solution for the Earth only, using a solar constant of 75% of the modern value (1036 W/m^2) for the 3.8 Ga Earth, calculated from Gough (1981). SOCRATES employs the correlated-k method for radiative transfer. Thermal radiation is treated via 17 bands (between 3.3 μm-10 mm), while stellar radiation is treated by 43 bands (0.20-20 μm). These are suitable for atmospheres dominated by a mixture of N_2 and CO_2 (from 1% to 20%), with up to 3.5% CH_4 (see tests in Eager-Nash et al. 2023), supporting surface pressures up to 10^6 Pa. These include CO_2 sub-Lorentzian line wings and CO_2 self-broadening. Collision induced absorption is included for: N_2–CH_4, N_2–N_2 and CO_2–CO_2 from HITRAN (Karman et al. 2019), and CH_4–CO_2 from Turbet et al. (2020). Line data are from HITRAN 2012 (Rothman et al. 2013). The solar spectrum for the climate solution is taken for a 2.9 Ga Sun spectrum from Claire et al. (2012), which has little difference in climate compared to a 3.8 Ga given the same solar constant is used.

We generate one climate state for all photochemical simulations, which is based on a 3.8 Ga Earth. We impose a climate with a composition of N_2, CO_2 and CH_4 for a 1 bar atmosphere. CO_2 is fixed at 10% to provide similar surface temperatures (Figure 2). CH_4 is fixed at 0.18%, while N_2 makes up the remaining atmosphere in each case. The assumption of using a mean climate state is justifiable as long-term modelling including a carbon cycle finds temperatures return to the abiotic steady state (e.g. Sauterey et al. 2020). We do not use cli-
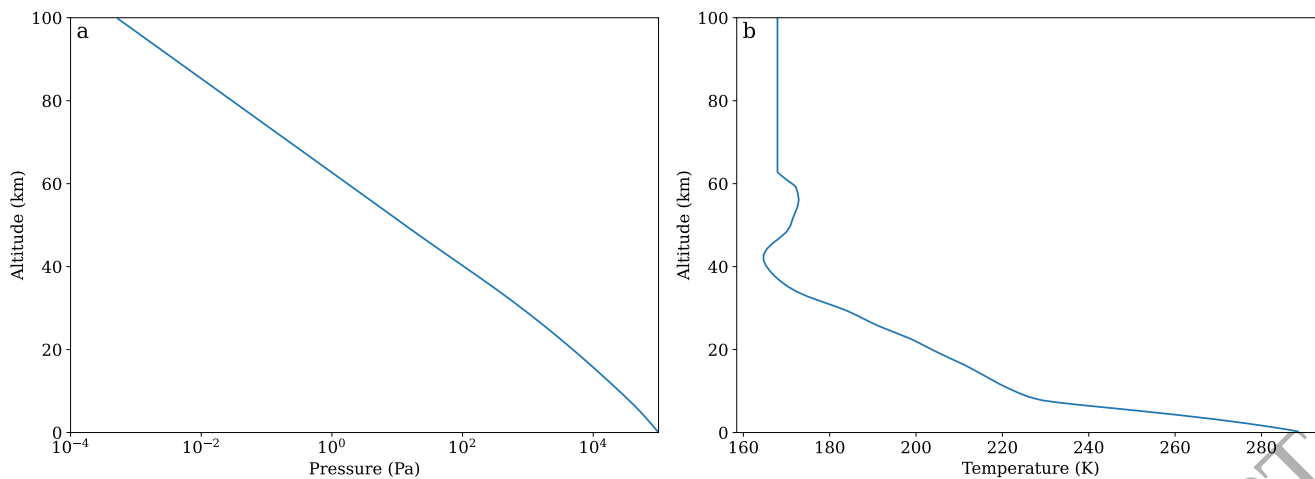
Figure 2. Pressure (a) and Temperature (b) vertical profiles used that were generated for 3.8 Ga Earth.

mate solutions for TRAPPIST-1e due to the limitations of our model with regards to representing a tidally locked planet. Using the planetary and orbital parameters of TRAPPIST-1e, we obtain a climate solution with a tropopause height that is too low (4.5km), caused by the low solar constant and a realistic climate solution would only be attainable when using a multi-column model to resolve the day and night sides.

4.2 Atmosphere-Ocean

The coupled atmosphere-ocean model with a given climate solution solves the continuity equation:

$$\frac{\partial n_i}{\partial t} = P_i - n_i L_i - \frac{\partial \Phi_i}{\partial z}, \tag{10}$$

where n_i is the number density of species i, P_i is the production rate of the species and L_i is the loss rate. Φ_i is flux of species i from vertical transport. This is solved for the atmosphere-ocean as a whole, with flux across the atmosphere–ocean boundary calculated using a stagnant boundary layer model (Liss & Slater 1974). PALEO is a flexible modelling tool using a single code, which uses a single solver to model various components of the Earth system together, such as the atmosphere and ocean in this work. Simulations were run for 3 to 800 million Earth years to allow the system to reach steady-state — when the reductant input is equal to reductant output through the sum of hydrogen escape and organic carbon burial. We now describe components of this model in more detail.

4.2.1 Photochemistry

We use two reaction networks, the full network containing reactions with carbon, hydrogen, oxygen, nitrogen and sulphur species and a reduced network containing just carbon, hydrogen and oxygen species. The species in each network are shown in Table 1, with the left side of the table showing the species in the reduced network only. The reduced network is used as it converges more readily, while the larger network is used to validate the results of the reduced network. Some species are assumed to be short-lived, meaning that their chemical lifetime is short enough to assume that the number

density can be determined directly from the chemical production and loss rates only. As the inclusion of short lived species can violate mass balance (Hu et al. 2012; Harman et al. 2015), we check the simulations for the conservation of atmospheric redox balance. The full network is composed of 399 reactions, compared to 207 in the reduced network, with the network derived from Gregory et al. (2021), which is shown in Appendix A. Reaction rates are calculated as described in Appendix A. Solar flux is split into 750 bins from 117.65 to 1000 nm, similar to the ATMOS model (Lincowski et al. 2018; Teal et al. 2022). This included the adoption of a two-stream approach to track stellar radiation for photolysis (Teal et al. 2022). Cross-sections and quantum yields come from the ATMOS open access repository[1] (Lincowski et al. 2018; Teal et al. 2022) and include the updated cross-sections for H_2O (Ranjan et al. 2020). The atmosphere extends to 100 km with 200 equally-spaced levels. The surface boundary conditions are shown in Table 1. As a result of uncertainties in the reductant input, we investigate a range of potential values of H_2 volcanic outgassing, $\Phi_{outgas}(H_2)$, from 0.1 to 100 Tmol/yr. Fluxes are given in units of Tmol/yr, which are global fluxes equivalent to an Earth sized planet. For the full network, we include a surface boundary flux of NO and CO, which represents the role of lightning (Harman et al. 2018). In the reduced network, we exclude both of these fluxes as we do not include nitrogen chemistry in this network and the CO flux would introduce an additional reductant input, discussed further in Section 4.2.4.

Tropospheric water vapour is fixed and decreases with temperature (Manabe & Wetherald 1967), with a prescribed surface relative humidity of 70 %. Above the tropopause water vapour may evolve from chemical sources and sinks, but when water vapour exceeds a critical relative humidity (100 %), it will condense and rainout.

The species can be deposited at the surface of the atmosphere as a result of either species dissolving into water droplets and subsequently raining out of the atmosphere, or through the particles directly settling from the atmosphere to the surface due to gravity or turbulence, which is known as dry deposition. Rainout follows the prescription described in (Giorgi & Chameides 1985), while dry de-

---

[1] https://github.com/VirtualPlanetaryLaboratory/atmos

Table 1. Species list and abiotic surface boundary conditions used in the model, which are either flux based or use a fixed mixing ratio. Fluxes are given in Tmol/yr and photochemical units (pu - molecules/cm^2/s), with a conversion rate of 1 pu equal to 2.7×10^{-10} used here. Species that are short lived are indicated. Dry deposition velocities values are also stated. The CHO network includes species on the left side of the table only.

[†]CO flux of this value is used for the full network only as part of lightning flux (equal to NO flux). For a sensitivity study in Section 5.3.4 a range of abiotic CO fluxes were used from 0.1 to 100 Tmol/yr, the same range as used for H$_2$.

Species	Short lived	Flux (Tmol/yr)	Flux (pu)	Mixing ratio (mol/mol)	Dry deposition velocity (cm/s)	Species	Short lived	Flux (Tmol/yr)	Flux (pu)	Mixing ratio (mol/mol)	Dry deposition velocity (cm/s)
CO_2				0.1		SO_2		0.802	2.97×10^9		1.0
N_2				0.88		H_2S		0.0802	2.97×10^8		
H_2O						NO		0.16	5.93×10^8		
CH_4		0.0802	2.97×10^8			CS_2					
H_2		0.1–100	3.70–3700×10^8			CS_2^*	y				
CO		0.16[†]	5.93×10^8			HS					
O_3					0.4	CS					0.01
O_2						HNO_2	y				
HO_2					1.0	HNO_3					0.2
H_2O_2					0.5	NO_2					3×10^{-3}
$O(^3P)$					1.0	N					
$O(^1D)$	y					HNO					1.0
OH					1.0	NO_3					
HCO					0.1	SO					
H_2CO					0.1	S					
H					1.0	$^1SO_2$	y				
CH_3						$^3SO_2$	y				
$^1CH_2$	y					HSO_3	y				
$^3CH_2$						SO_3					
CH_3O					0.1	H_2SO_4					
C_2H_6					1×10^{-5}	HSO					1.0
C_2H_5						S_2					
C_2H_4						OCS					0.01
CH_3O_2						S_3					
C_2H_2						S_4					
CH_3CHO					0.1	S_8					
C						OCS_2	y				
CH						N_2O_5					
CH_2CO					0.1	HO_2NO_2					0.2
CH_3CO					0.1	N_2O					
C_2H						HCS					
C_2											
C_2H_3											
C_2H_2OH											
C_2H_4OH											

position is modelled at the lowest atmosphere level, with deposition flux, Φ^{dep} (molecules/cm^2/s) for species i is calculated as

$$\Phi_i^{dep} = n_i v_i^{dep}, \tag{11}$$

where v^{dep} is the deposition velocity. This represents the free fall of species out of the atmosphere. Eddy diffusivity models the upward vertical mixing of the atmosphere and is calculated for species i as:

$$\Phi_i^{eddy} = -KN\frac{\partial}{\partial z}\frac{n_i}{N}, \tag{12}$$

where K is the eddy diffusion coefficient plotted in Figure A1, N is the total number density of the atmosphere at height z.

Escape and molecular diffusion of molecular and atomic hydrogen follow the procedure outlined in Hu et al. (2012) and Ranjan et al. (2020). We follow the implementation used in Hu et al. (2012),

which combines diffusion and escape as linked processes. We include the escape of atomic and molecular hydrogen for an N_2-dominated atmosphere, and use the gravitational acceleration of 9.81 and 9.12 m/s^2 for Earth and TRAPPIST-1e simulations respectively, with the latter consistent with values used in other studies (e.g. Fauchez et al. 2020).

The top-of-atmosphere spectra received by the planet used in this work are shown in Figure 3. The solar spectrum for 3.8 Ga is generated from Claire et al. (2012), while the quiescent spectrum for TRAPPIST-1 uses the spectrum from Peacock et al. (2019). The mean-flaring spectrum is generated using the same approach described in Ridgway et al. (2022) using the TRAPPIST-1 spectrum from the Mega–MUSCLES survey (Wilson et al. 2021).
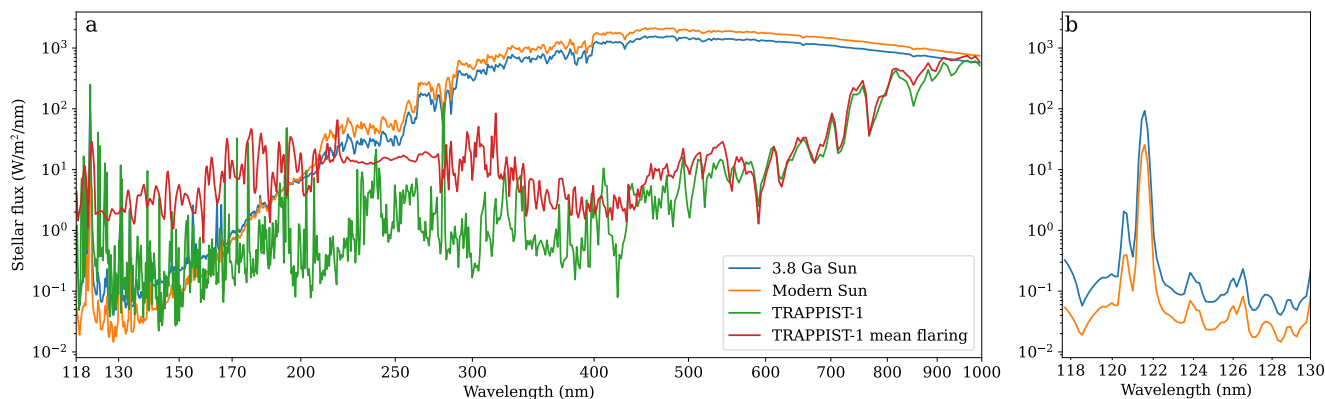
Figure 3. Top-of-atmosphere spectra used for Earth by the modern and 3.8 Ga Sun and TRAPPIST-1e for a quiescent and mean-flaring TRAPPIST-1 spectrum. (a) shows the spectra for the full range of fluxes for the photochemical model, while (b) shows the flux around Lyman-alpha for the 3.8 Ga and modern Sun spectra. The spectra from the modern Sun come from the Atmos open repository (Teal et al. 2022), while the 3.8 Ga Sun spectra comes from Claire et al. (2012). The TRAPPIST-1 spectra is from Peacock et al. (2019), while the flaring spectra uses the spectrum from Wilson et al. (2021) and includes a temporally-averaged spectrum which describes a regularly flaring star based on Ridgway et al. (2022).

Table 2. Solubility and piston velocity values used within the model.

| Species	Solubility (mol/m³/Pa)	Piston velocity (m/day)
CO_2	1.0×10^{-2}	4.8×10^{-2}
CH_4	1.4378×10^{-5}	4.8
H_2	8.0106×10^{-6}	11.23
CO	1.027×10^{-5}	4.147
O_2	1.2×10^{-5}	4.8

4.2.2 Ocean

A single box ocean is connected to the atmosphere, with reservoirs of species connected between the atmosphere and ocean via diffusion. A single box ocean is used as we assume a biosphere that is globally spread, which follows approaches used in Kharecha et al. (2005); Ozaki et al. (2018); Nicholson et al. (2022). Using a similar procedure to Kharecha et al. (2005) the diffusion is determined by a piston velocity and solubility coefficient, with values given in Table 2. The flux across the ocean-atmosphere boundary for species X, $\Phi(X)$ is then:

$$\Phi(X) = v_p(X) \times (\alpha(X) \times pX - [X]_{aq}) \times C, \quad (13)$$

where $v_p(X)$ and $\alpha(X)$ are the piston velocity and the Henry's solubility coefficient of X, respectively, pX is the surface partial pressure of X and $[X]_{aq}$ is the ocean concentration of X. C is a constant for unit conversion to obtain a flux in mol/yr.

In the abiotic simulations and biotic simulations without CO consumers, the ocean includes a CO sink, following the reaction described in (Harman et al. 2015), taking the form:

$$CO + H_2O \longrightarrow H_2 + CO_2, \quad (14)$$
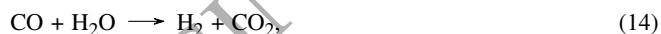
with the rate of removal of CO calculated as $\tau[CO]$, where τ is a timescale of removal, with a value of 10^{-4} used here, and [CO] is the oceanic concentration of CO.

4.2.3 Biosphere

We couple a simple ocean with a biosphere component to the 1D atmosphere model, which is shown schematically in Figure 1. The primary production from this biosphere comes from the consumption of H_2 and CO, which reach the ocean through the diffusion of these species from the atmosphere.

The number of mols of H_2/CO required to produce energy for the biomass pathway can be measured experimentally. For methanogens, it has been measured that for every 10 mols of CO_2 that are metabolised, 1 mol of CO_2 is converted to biomass through anabolism (Schonheit et al. 1980; Fardeau & Belaich 1986; Morii et al. 1987). The proportion of the total metabolism by a species in the form of anabolism is termed the growth rate, μ. For the purposes of this work, it is assumed that anoxic H_2 and CO consuming metabolisms have a growth rate of 0.1, while for anoxic photosynthesisers, a growth rate of 1.0 is used as they extract energy directly from the host star to fix carbon. The growth rate has only a minor role in the evolution of the atmosphere, provided the burial fraction is low (Section 5.3.3).

Secondary consumers recycle organic carbon back to CH_4. However, this process is not 100% efficient and some fraction of the biomass is buried, which may limit the production of CH_4. The rate of organic carbon burial, x, is an unconstrained parameter for exoplanets. However, it has thought to have decreased over Earth history, with a modern value of 0.2% (Berner 1982). We use a value of 1% in these simulations unless otherwise stated. This value may have been similar to the Archean, based on measurements of carbon burial in anoxic waters (Arthur et al. 1994). The sensitivity to various recycling rates is analysed in Section 5.3.3, ranging from no recycling to 100% efficient recycling. The growth rate and organic carbon burial rate are not considered for the oxic metabolisms. However, a sensitivity study of the burial rate and growth rate for the other parameters shows that these only have a minor effect when the burial rate is above 10%, see Section 5.3.3.

Following similar treatment in Kharecha et al. (2005) and Ozaki et al. (2018), it is assumed that either H_2 or CO are the limiting factors in primary productivity for anoxic metabolisms. Oxic metabolisms are limited by the either availability of O_2 or CO/CH_4 depending on the metabolism. The net primary productivity (NPP), in terms of moles of H_2/CO equivalent consumed by the anoxic metabolisms is:

$$\Phi_{\text{bio}}(\text{NPP}) = \sum_X \tau_{\text{bio}}([X]_{aq} - [X]_{aq}^{lim}), \tag{15}$$

for the sum of limiting species X for each metabolism (H_2 and CO) and $[X]_{aq}^{lim}$ is the limiting concentration of species X, which the biosphere is unable to draw concentrations below (set here as 4.6×10^{-7} mol/m^3). τ_{bio} is the timescale for the biological reaction, which is assumed to be 10^4 yr^{-1}. Provided this timescale is high enough to reduce ocean concentrations to $[X]_{aq}^{lim}$, which is expected for a global biosphere, this parameter has no effect on the atmospheric configuration. Of this flux of gas consumed some fraction of this flux goes towards producing organic carbon. This proportion is known as the growth rate, μ, where we assume the remaining fraction is used for producing energy to create organic carbon (see Section 3). Thus, the proportion of organic carbon produced from $\Phi_{\text{bio}}(\text{NPP})$ is

$$\Phi_{\text{bio}}(\text{CH}_2\text{O}) = \frac{1}{2}\mu \times \Phi_{\text{bio}}(\text{NPP}). \tag{16}$$

The factor of half comes from the number of moles of X required to form one mole of organic carbon equivalent (CH_2O). The burial rate is then:

$$\Phi_{\text{burial}}(\text{CH}_2\text{O}) = x\Phi_{\text{bio}}(\text{CH}_2\text{O}), \tag{17}$$

where x is the burial rate, the fraction of organic carbon that does not get recycled. The biotic CH_4 flux from these metabolisms is then the difference between these two fluxes:

$$\begin{aligned}\Phi_{\text{bio}}(\text{CH}_4) &= \frac{1}{4}\Phi_{\text{bio}}(\text{NPP}) - \frac{1}{2}\Phi_{\text{burial}}(\text{CH}_2\text{O}) \\ &= \frac{1}{4}(1 - x\mu)\Phi_{\text{bio}}(\text{NPP}),\end{aligned} \tag{18}$$

with the fractions used to convert fluxes to CH_4 equivalent fluxes.

In this work, two ecosystems are predominantly used:

(i) Ecosystem 1: preoxygenic anoxic metabolisms only, including anoxic H_2 and CO consumers (Equations 1–4) and secondary consumers (Equation 5)

(ii) Ecosystem 2: ecosystem 1 plus oxic metabolisms that metabolise O_2 with CH_4 or CO (Equations 8 & 9)

4.2.4 Global redox balance

To conserve global redox balance in our model, we follow similar logic to Harman et al. (2015) to ensure our atmosphere-ocean boundary conserves redox. In our model, the global redox state is conserved by balancing

$$\Phi_{\text{outgas}}(\text{Red}) = \Phi_{\text{esc}}(\text{H}_2) + 2\Phi_{\text{burial}}(\text{CH}_2\text{O}), \tag{19}$$

where $\Phi_{\text{outgas}}(\text{Red})$ is the reductant outgassing through species such as H_2. $\Phi_{\text{esc}}(\text{H}_2)$ is the hydrogen escape flux and $\Phi_{\text{burial}}(\text{CH}_2\text{O})$ is the burial of organic carbon, written in terms of its H_2 equivalent redox potential, with reducing fluxes on the left and oxidising fluxes on the right. We do not include in this oxidative weathering or iron and sulphur related burial. Meanwhile redox balance in the ocean is conserved when

$$\Phi_{\text{dep}}(\text{Red}) = \Phi_{\text{dep}}(\text{Ox}) + 2\Phi_{\text{burial}}(\text{CH}_2\text{O}), \tag{20}$$

$\Phi_{\text{dep}}(\text{Ox})$ and $\Phi_{\text{dep}}(\text{Red})$ is the wet and dry deposition of oxidising

and reducing species respectively at the atmosphere-ocean boundary. This means that the net deposition at the atmosphere-ocean boundary must equal the organic carbon burial flux. To account for this, the ocean cycling of species that are utilised by the biosphere are separated from the deposition of other species. Species used by the biosphere and abiotic chemistry (Table 2) are tracked in the ocean. The net redox flux of these species from biological reactions (through diffusion into and out ocean) is then balanced by the organic carbon burial:

$$4\Phi_{\text{dep}}(\text{CH}_4) + \Phi_{\text{dep}}(\text{H}_2) + \Phi_{\text{dep}}(\text{CO}) = 2\Phi_{\text{dep}}(\text{O}_2) + 2\Phi_{\text{burial}}(\text{CH}_2\text{O}). \tag{21}$$

The remaining deposition fluxes must then be redox balanced:

$$\Phi'_{\text{dep}}(\text{Ox}) = \Phi'_{\text{dep}}(\text{Red}), \tag{22}$$

where we denote Φ'_{dep} as the total deposition fluxes not traced in the ocean. Following the treatment in (Harman et al. 2015), as these fluxes are rarely equal, a balancing flux of H_2 or O_2 is added back into the atmosphere so that this surface exchange is redox neutral. In the case a net reducing deposition surface sink, an equivalent flux H_2 is added back into the atmosphere at the surface, while in the case of a net oxidising surface deposition, an equivalent flux of O_2 is used instead.

To maintain consistency in the reductant input for the full network and the reduced network, surface boundary flux of H_2S is included in the flux calculation for surface redox balance, such that the net reductant input from H_2S is zero. This ensures that the net reductant input is determined by the H_2 and CH_4 abiotic fluxes only. SO_2 is considered a redox neutral species, so does not affect the redox balance, while the combined lightning fluxes of CO and NO have an equal and opposite redox state, so also do not contribute to the redox balance.

4.3 Synthetic spectra

Synthetic spectra were generated using the Planetary Spectrum Generator (PSG) (Villanueva et al. 2018), adopting the parameters of TRAPPIST-1e (Agol et al. 2021). The following species were included to generate the spectrum: O_2, CH_4, N_2, C_2H_6, O_3, CO_2, CO, H, H_2, O, C_2H_2, C_2H_4. From this, we can investigate the differences in transmission spectrum between biotic and abiotic configurations to assess the detectability of a potential biosphere of the form modelled here. Synthetic observations were then created using PandExo (Batalha et al. 2017). These were generated for the JWST NIRSpec PRISM instrument mode.

5 RESULTS

We now present results of abiotic simulations of TRAPPIST-1e, comparing these to simulations of the 3.8 Ga Earth, showing the importance of reductant input in abiotic O_2 levels. Following this, we present results from the biotic configurations for TRAPPIST-1e, initially benchmarking the coupled atmosphere-ecosystem model against Kharecha et al. (2005) on Earth, and subsequently comparing the differences between early Earth biospheres on Earth and on a hypothetical TRAPPIST-1e. Finally, we show transmission spectra for TRAPPIST-1e for a range of both biotic and abiotic configurations.
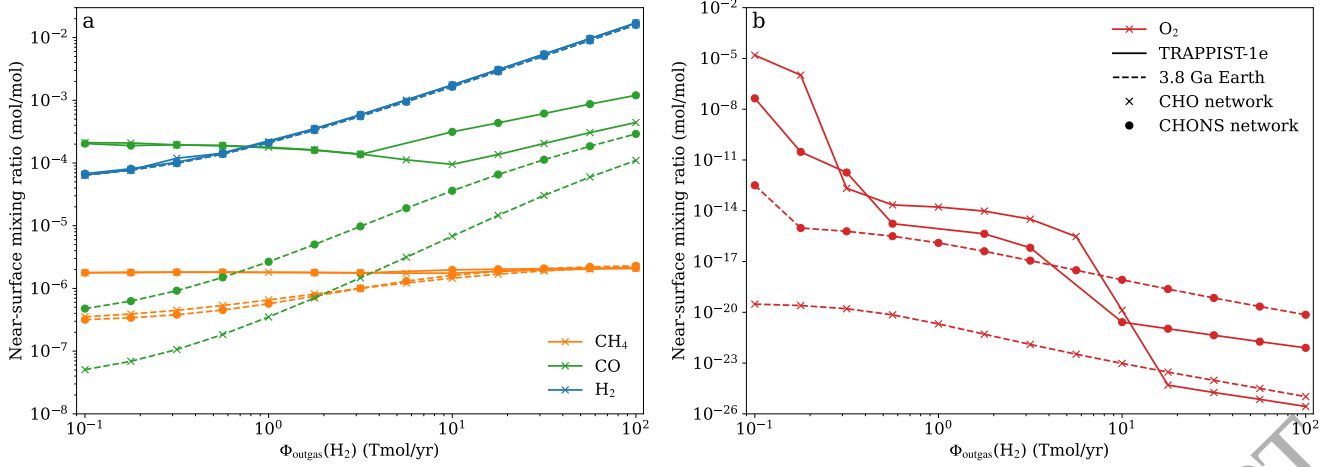
Figure 4. Near-surface (250 m above the surface) mixing ratios for abiotic configurations of TRAPPIST-1e (solid) and Earth irradiated by a 3.8 Ga Sun (dashed) as a function of H_2 input. The full grid of simulations is shown for the reduced network (crosses), while a subset of the network is plotted as circles.
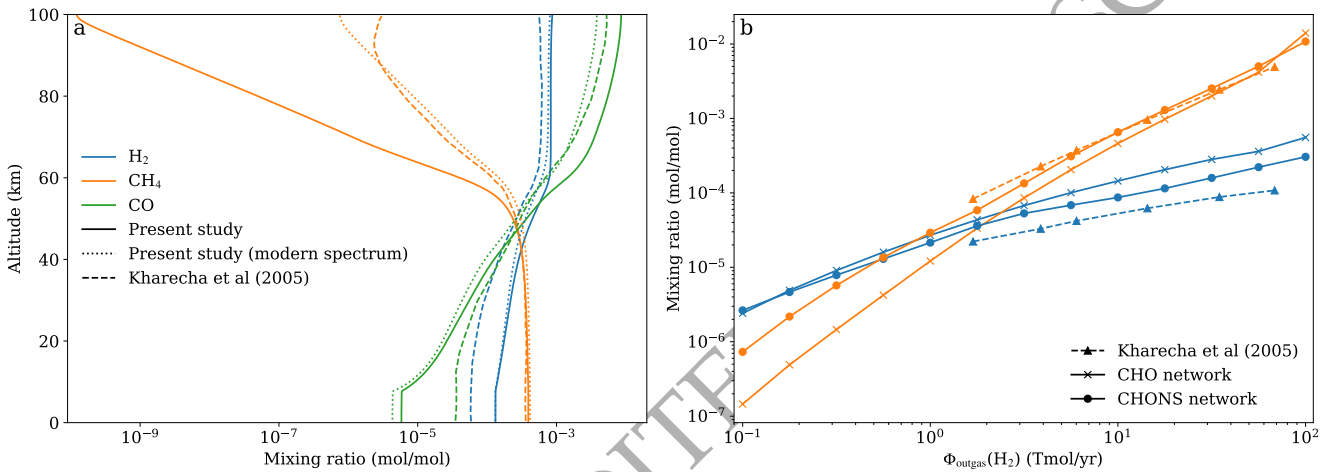

Figure 5. Comparison to Kharecha et al. (2005). (a) shows mixing ratios vs altitude for case 2 biosphere in Kharecha et al. (2005) (dashed lines), equivalent to their Fig. 7B. This is compared to simulations in this work of the 3.8 Ga Solar spectrum (Claire et al. 2012) (solid line) and the modern Solar spectrum (dotted lines) from ATMOS (Teal et al. 2022). (b) shows the near-surface mixing (250 m above the surface) ratios of CH_4 and H_2 in this work (solid lines) and data from Table 2 in Kharecha et al. (2005) for their case 3 biosphere (dashed lines). The case 2, (a), and 3, (b), biospheres have growth rates of 0.1 and 1.0 for H_2 consumers respectively, while the CO consumer growth rate is 0 for both cases. The organic carbon burial rate is 2 %. The CO_2 near-surface mixing ratio is 2.5 %. Our simulations are shown for the reduced network in (a), while (b) shows the full network (circles) and reduced network (crosses).

5.1 Abiotic O_2 production

Figure 4 shows a comparison of an abiotic configuration of Earth and TRAPPIST-1e, with near-surface mixing ratios of key gases as a function of H_2 input. In the rest of the paper, near surface refers to 250 m above the surface as this is the lowest atmospheric level. This is shown for the full and reduced network. H_2 is the major hydrogen-bearing species and thus its concentration increases with input, which allows hydrogen escape to balance input. This trend is similar for both Earth and TRAPPIST-1e. CO is higher in the TRAPPIST-1e case because of CO_2 photolysis and a lack of tropospheric OH from H_2O photolysis to catalyse the recombination of the CO_2 photolysis products (Harman et al. 2015). Near-surface O_2 is shown in Figure 4b.

Reductant input plays an important role in determining abiotic O_2 mixing ratios. At low reductant input, $\Phi_{outgas}(H_2) < 10$ Tmol/yr, O_2 becomes significantly higher for the TRAPPIST-1e case compared to the Earth analogue. This is because reductant input is lower than O_2 production from CO_2 photolysis. When reductant input is higher than O_2 production from CO_2 photolysis, O_2 returns to levels comparable to the Earth case.

The reduced and full chemical network show similar trends in atmospheric mixing ratio. H_2 and CH_4 remain nearly identical between the two simulations. CO is higher for both TRAPPIST-1e (when $\Phi_{outgas}(H_2) > 3.16$ Tmol/yr) and the Earth. This is due to the CO flux from lightning in the full network, which is not included in the reduced network. This is not observed at $\Phi_{outgas}(H_2) \leq$
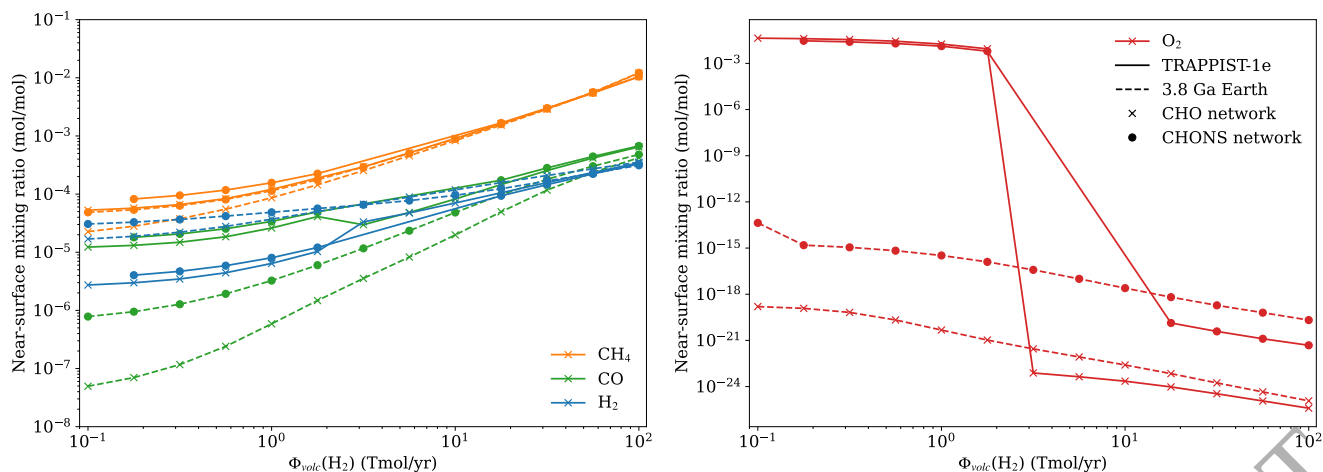
Figure 6. Comparison of a hypothetical H_2 and CO consuming ecosystem (ecosystem 1) on TRAPPIST-1e (solid lines) compared to a 3.8 Ga Earth (dashed lines). (a) and (b) show near-surface (250 m above the surface) mixing ratios for key gases. The full grid of simulations is shown for the reduced network (crosses), while a subset of the network is plotted as circles.

3.16 Tmol/yr for TRAPPIST-1e as the CO source from CO_2 photolysis is much larger. O_2 shows very similar trends between the full and reduced network. For TRAPPIST-1e, the O_2 predictions at $\Phi_{outgas}(H_2) > 3.16$ Tmol/yr are consistent between both networks. For Earth, abiotic O_2 is higher when the full network is used, which produces values closer to those found in Kasting (1990). The lower values in the reduced network are similar to those quoted in Ranjan et al. (2023). As these O_2 values are very low, differences are likely to be caused by the numerics of the solver.

5.2 Benchmarking of atmosphere ecosystem model

We now consider the effects of a biosphere composed of anoxic metabolisms of H_2 and CO. We first compare our model simulations to Kharecha et al. (2005), who implemented a similar ecosystem model. Figure 5 shows a comparison to their results for a H_2 and CO consuming biosphere with a 2% organic carbon burial rate. For $\Phi_{outgas}(H_2) = 6.02$ Tmol/yr (see Figure 5a), the mixing ratio profiles of CH_4 are similar up to 70 km (compare solid and dashed lines), above which we predict much less CH_4, due to the difference in solar spectrum. We repeat our runs with the modern Earth spectrum (dotted lines), which shows better agreement (compare dotted and dashed lines in Figure 5a). The sharper falloff of CH_4 with the 3.8 Ga spectrum is caused by the high UV flux around Lyman-alpha (Figure 3b). The H_2 mixing ratio profiles are similar for both cases, while the CO mixing ratio is drawn down to lower values near the surface in our model, but reaches higher abundances at the top-of-atmosphere. Figure 5b shows the near-surface mixing ratios of H_2 and CH_4 for their case 3 biosphere, with the CH_4 mixing ratio showing strong agreement with Kharecha et al. (2005). The difference between the full and reduced reaction network are minimal here, with the only difference at low reductant input, where CH_4 concentrations are marginally higher in the full network.

5.3 Pre-photosynthetic biospheres on TRAPPIST-1e

We now show the effect of a hypothetical H_2 and CO consuming biosphere on the atmosphere for a planet orbiting TRAPPIST-1, com-

pared to the young Sun. We show results from ecosystem 1 (anoxic H_2 and CO consumers) and subsequently ecosystem 2 (anoxic H_2 and CO consumers and oxic CH_4 and CO consumers) for simulations with high O_2 mixing ratios.

5.3.1 Ecosystem 1

Figure 6 shows the near-surface (250 m above the surface) mixing ratios for the biotic configuration with ecosystem 1 (anoxic H_2 and CO consumers only). The TRAPPIST-1e case has CH_4 at higher concentrations near the surface compared to Earth, which is related to the lower OH concentration in the troposphere. The general behaviour of CH_4 is similar for both cases, with CH_4 now the dominant reductant species, and its concentration largely determined by the balance of reductant input with hydrogen escape. The most notable difference however is the relatively high near-surface O_2 (around 1–5%) at low $\Phi_{outgas}(H_2) < 3.16$ Tmol/yr.

The difference in near surface O_2 mixing ratios between Ecosystem 1 and the abiotic case is caused by the reduction in atmospheric CO by CO-consuming organisms. The formation of O_2 is predominantly from the combination of O in the upper atmosphere (Figure 7d), which originates from CO_2 photolysis. This can oxygenate the atmosphere, when CO is consumed by the biosphere. The reduction in atmospheric CO due to Ecosystem 1 compared to the abiotic case (Figure 7a) leads to the rate of reaction of CO with OH dropping by orders of magnitude below 40 km (Figure 7c). The reaction of CO + OH is orders of magnitude higher in the abiotic case compared to reactions of CH_4 and H_2 with OH (Figure 7c), and is key to the catalytic loss of O (Harman et al. 2015), with associated rates shown in Figure 7d. The oxidising power of O in the upper atmosphere is relatively small compared to OH, shown by its reaction with H_2 and CH_4 in Figure 7c. The effect of CO-consuming organisms is further demonstrated by the removal of the CO metabolism from the Ecosystem 1 simulations.

Figure 8 shows that the removal of CO-consuming metabolisms leads to the disappearance of the high O_2 state. The lack of this metabolism leads to CO reaching mixing ratios more comparable to the abiotic case, leading to low levels of O_2 (less
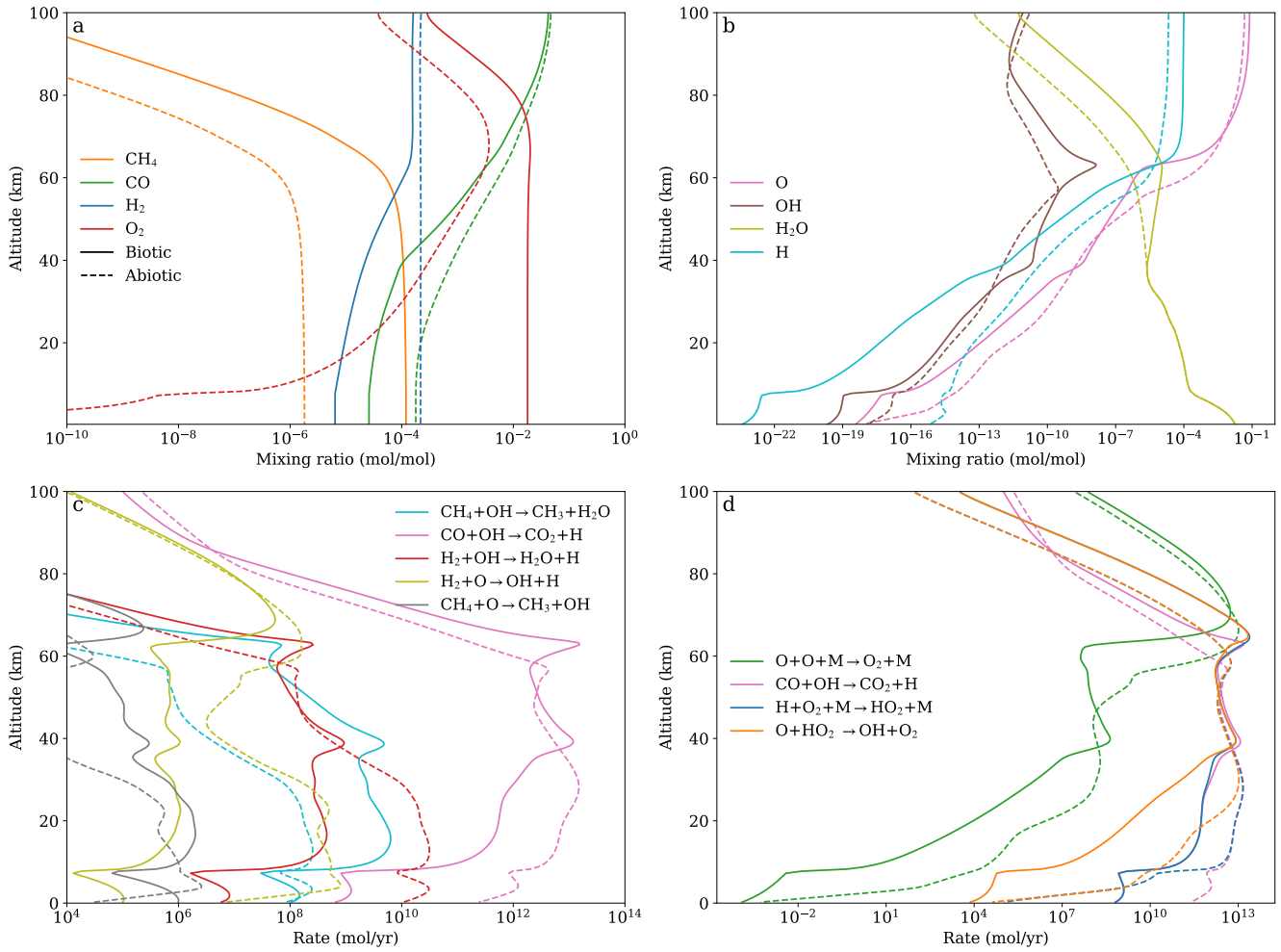
Figure 7. Comparing the ecosystem 1 biotic (solid lines) and abiotic (dashed lines) configuration at $\Phi_{outgas}(H_2) = 1.0$ Tmol/yr, with (a) and (b) showing vertical mixing ratios of selected species and (c) and (d) showing the reaction rates for selected reactions.
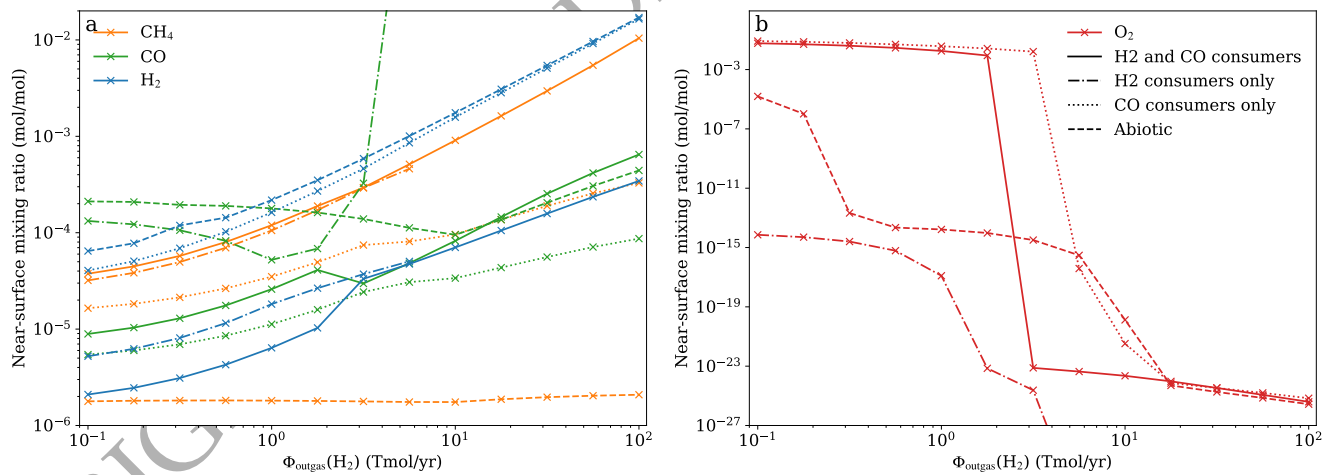
Figure 8. Showing the near-surface (250 m above the surface) mixing ratios for selected gases for the full ecosystem 1 (H_2 and CO consumers, solid lines), H_2 consumers only (dash-dotted), CO consumers (dotted) and the abiotic configuration (dashed).
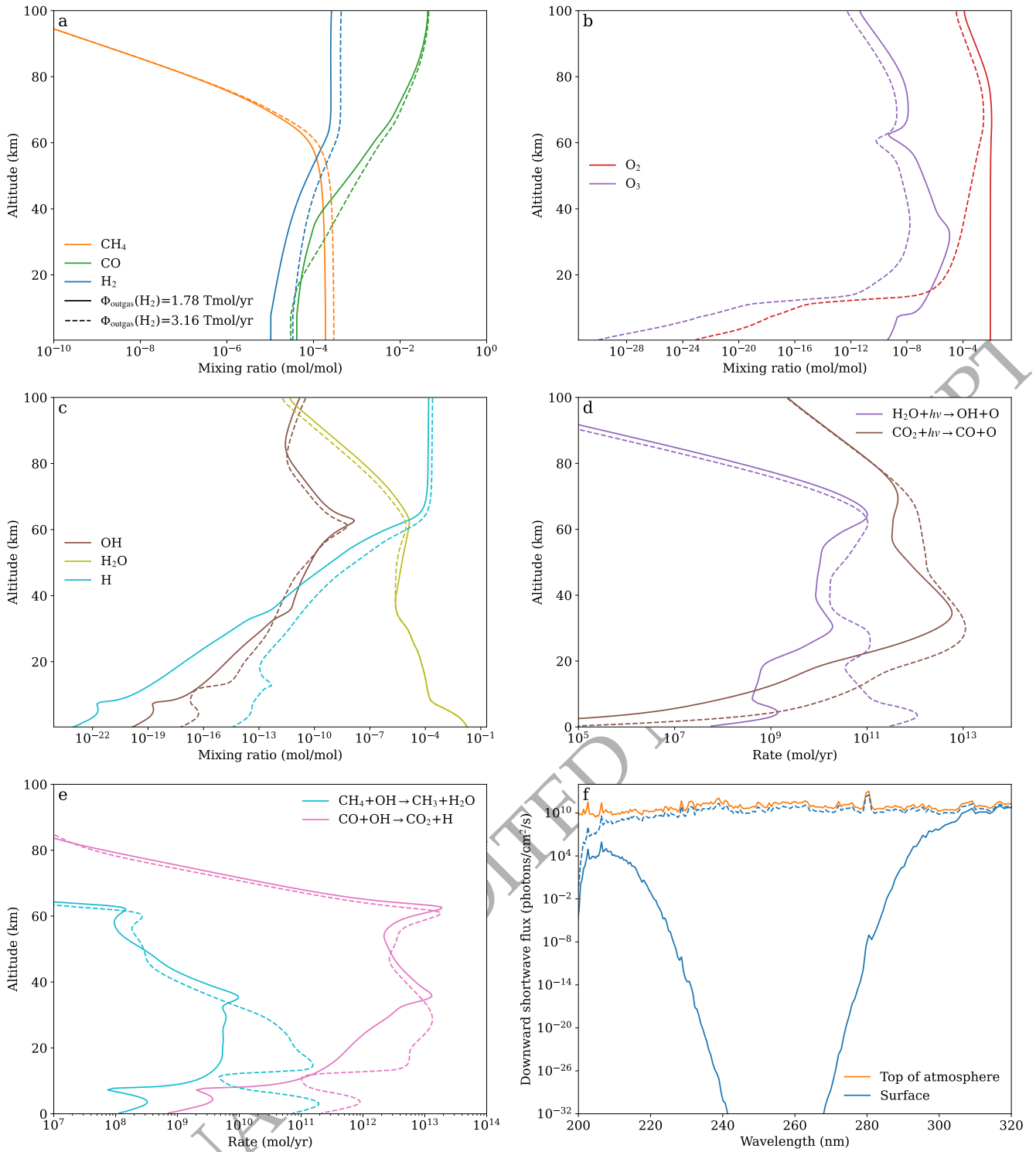
Figure 9. Differences between the low O_2 state at $\Phi_{outgas}(H_2) = 1.78$ Tmol/yr (solid lines) and the high O_2 scenario at $\Phi_{outgas}(H_2) = 3.16$ Tmol/yr (dash-dotted lines). (a), (b) and (c) show gas mixing ratios, while (d) and (e) show reaction rates. (f) shows the downward shortwave flux at the top of atmosphere (TOA) and the surface.
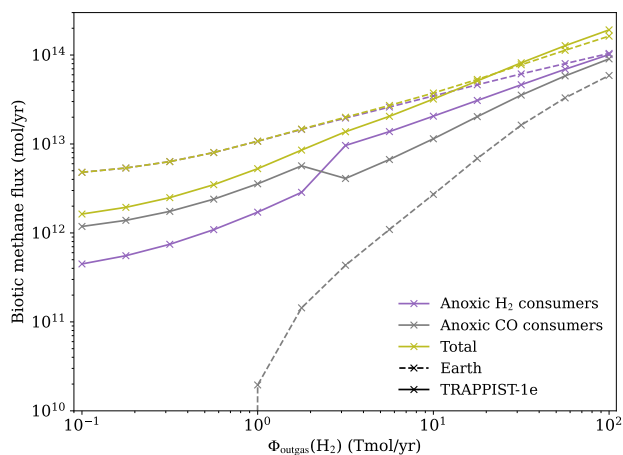
Figure 10. Shows the CH_4 production rate from ecosystem 1 for the 3.8 Ga Earth (dashed) and TRAPPIST-1e (solid) case. The CH_4 production rate is split between anoxic H_2 (purple) and CO (grey) consumers. the total of these is also shown (green) This plot used simulations with the reduced network.

than 10^{-14} mol/mol). However, as reductant input increases above 3.16 Tmol/yr, CO undergoes a runaway, increasing sharply with reductant input. This merits further investigation but requires testing and validation of our model for extreme CO mixing ratios, so we reserve a full investigation for future work. Meanwhile, the presence of CO-consuming metabolisms only, without H_2-consuming metabolisms, retains the original high O_2 state at low reductant input, but with a lower CH_4 and higher H_2 abundance. However, the high O_2 state extends to slightly higher reductant inputs than for when H_2-consuming metabolisms are present. This is likely due to CH_4 becoming the main H-bearing reducing species as opposed to H_2, meaning the rate of CO production increases, which, in turn, decreases the reductant input required to reduce the high O_2 state. As with the CO runaway, this requires further detailed investigation which we will perform in a follow up study.

The high O_2 disappears when reductant input increased compared to the O_2 production from CO_2 photolysis. Figure 9 compares the differences between this oxidised state at $\Phi_{outgas}(H_2) = 1.78$ Tmol/yr and the more familiar low O_2 state at $\Phi_{outgas}(H_2) = 3.16$ Tmol/yr. At $\Phi_{outgas}(H_2) \leq 1.78$ Tmol/yr, the high levels of O_2 is the product of CO_2 photolysis followed by the combination atomic oxygen:

$$CO_2 + h\nu \longrightarrow CO + O, \qquad (23)$$

$$O + O + M \longrightarrow O_2 + M. \qquad (24)$$

When the reductant input is low, O_2 accumulates faster than it can be reduced by the reductant input, leading to an accumulation of O_3 (dotted lines in Figure 9b). This O_3 shields the tropospheric UV flux (at $\Phi_{outgas}(H_2) = 1.78$ Tmol/yr) and reduces the photolysis of H_2O via:

$$H_2O + h\nu \longrightarrow OH + H, \qquad (25)$$

which further reduces the loss mechanisms for O_2 as well as CO and CH_4. The high levels of O_2 in the atmosphere lead to low levels of H_2, causing the low H_2-consumer productivity at these fluxes with CO-consumers contributing the largest CH_4 flux, shown in Figure 10.

When $\Phi_{outgas}(H_2) \geq 3.16$ Tmol/yr, the reductant input is large

enough to significantly reduce the O_2 concentration to levels seen in the Earth case. The subsequent lack of O_3 no longer shields the troposphere from UV radiation, increasing H_2O photolysis in this region. Increased OH leads to lower CO and CH_4 abundances. The reduction of O_2 down to levels that are comparable to the Earth case allows for a higher H_2 abundance, which consequently leads to an increase in H_2 consumption, which becomes the dominant source of biological CH_4 production over CO consumption (Figure 10).

The overall biotic CH_4 flux is generally smaller on TRAPPIST-1e compared to the Earth (Figure 10), which can be attributed to the slower rate of photochemically driven destruction of CH_4 via OH (Segura et al. 2005). At low reductant inputs ($\Phi_{outgas}(H_2) < 10$ Tmol/yr) the CH_4 flux is significantly larger than the reductant outgassing rate, showing the importance of atmospheric recycling of CH_4 back to H_2 and CO. As this process is slower for TRAPPIST-1e, the biological CH_4 flux is lower, while the atmospheric CH_4 concentration is up to a factor of two larger. The CH_4 production from CO consumers is more comparable to the H2 consumers as a result of the higher mixing ratios of CO on TRAPPIST-1e compared to the Earth (Figure 6a). When O_2 is high, the CH_4 flux from CO consumers is higher than for H_2 consumers.

The full and the reduced reaction network, both show very similar predictions for the atmospheric composition. This is shown in Figure 6. Most significantly, the high O_2 state is reproduced with both configurations. As we have now shown that the reduced and full network show very similar results for the abiotic configurations, the reproduction of Kharecha et al. (2005) and for ecosystem 1 for TRAPPIST-1e and the Earth, moving forward we use the reduced network only.

5.3.2 Ecosystem 2

The presence of high abundances of O_2 provides an energy source for potential ecosystems. The effect of including oxic CH_4 and CO consumers alongside the metabolisms in Ecosystem 1 (Ecosystem 2) is shown in Figure 11 for $\Phi_{outgas}(H_2) \leq 1.78$ Tmol/yr. Figure 11a shows that O_2 concentrations could be drawn down to near-surface mixing ratios of the order 10^{-5}, whilst also drawing down CH_4 concentrations slightly. However, CO is found to rise by up to an order of magnitude (Figure 11a and Figure 12a). In this ecosystem, the anoxic and oxic CO consumers dominate the biological productivity, as the oxic CH_4 and anoxic H_2 consumer productivity is low, shown in Figure 11b. The productivity of anoxic CO consumers is higher than in Ecosystem 1 due to the increased atmospheric CO concentration (Figure 11a).

The rise of atmospheric CO is a result of an increase in the photolysis rate of CO_2, caused by the reduction in O_2 and thus O_3 abundance, shown in Figure 12b at $\Phi_{outgas}(H_2) = 0.1$ Tmol/yr. The higher CO concentration in the atmosphere also contributes to the drop in O_2, but the presence of CO consuming species, which consume more CO than O_2 (anoxic CO consumers have a higher rate than oxic CO consumers,shown in Figure 11), prevents O_2 from falling further. The reduction in O_2 also leads to an increase in the production of tropospheric OH, which contributes to the lower CH_4 abundance in Ecosystem 2. At a high enough reductant input, $\Phi_{outgas}(H_2) > 0.56$ Tmol/yr, the presence of oxic metabolisms is sufficient to reduce O_2 to less than 10^{-19} mol/mol. Here, the biological rates of these metabolisms also go to zero, showing the sensitivity of this regime.
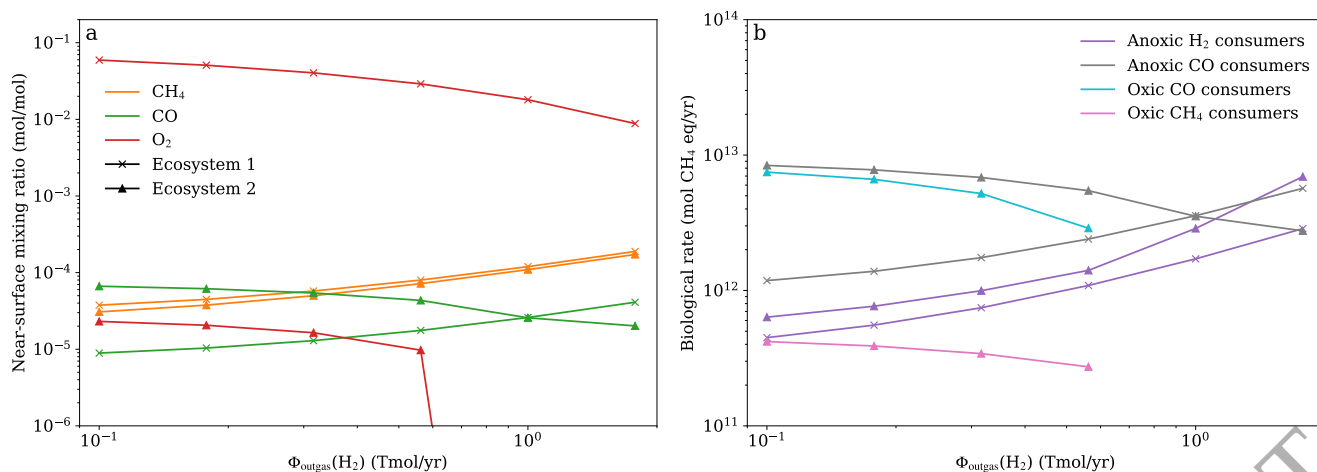
**Figure 11.** Comparison between ecosystem 1 and 2 at low reductant inputs, which produced high O_2 concentrations. (a) shows the near-surface (250 m above the surface) mixing ratios for key gases for ecosystem 1 (crosses) and ecosystem 2 (triangles). (b) shows the rate of biological reactions from ecosystem 2 in units of moles of CH_4 equivalent - in terms of CH_4 production for anoxic reactions and in terms of reductant consumption (as either CO or CH_4) in the oxic reactions. Above $\Phi_{outgas}(H_2)$= 1.78 Tmol/yr, the O_2 concentration drops and oxic metabolisms can no longer function, thus becomes identical to ecosystem 1 and is not shown.
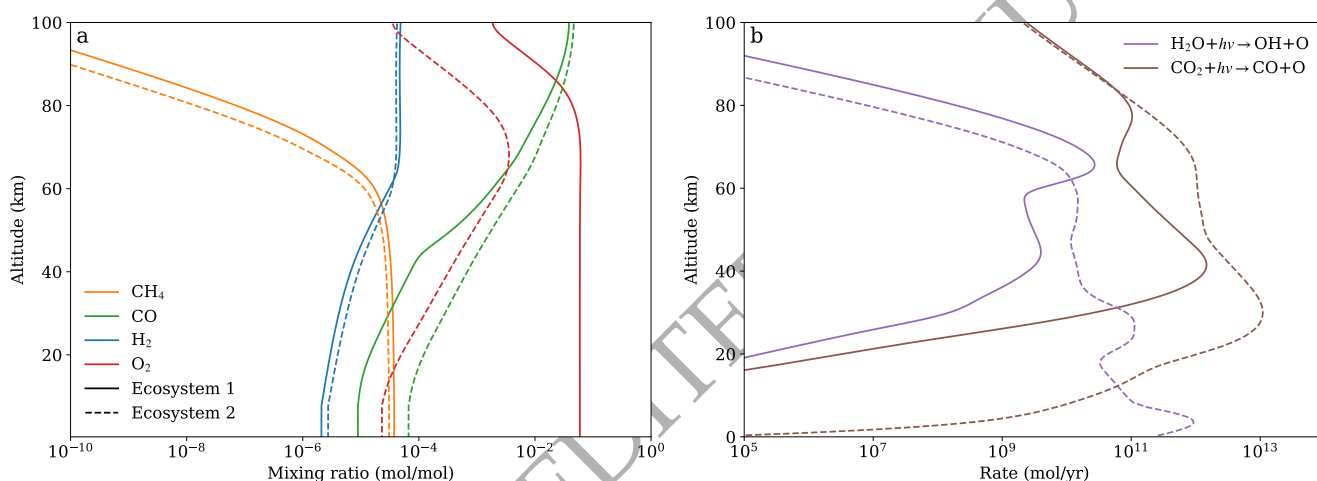
Figure 12. Comparison between the atmospheric composition (a) and photolysis rates (b) produced by ecosystem 1 (solid) and ecosystem 2 (dashed) when $\Phi_{outgas}(H_2)$= 0.1 Tmol/yr.

5.3.3 Anoxygenic photosynthesis and carbon burial

We now consider the potential impacts of anoxygenic photosynthesis compared to ecosystems that obtain energy through catabolism. That is to say that the growth rate becomes 100%, as opposed to the 10% that was assumed previously. To consider the effects of this, we investigate the change in growth rate alongside the sensitivity to the rate of organic carbon burial. We find that anoxygenic photosynthesis using H_2 and CO is unlikely to lead to significant changes in the atmospheric composition unless the organic carbon burial rate is low.

Ecosystems with low growth rates, such as prephotosynthetic biospheres are relatively unaffected by the fraction of biomass that is buried. For a growth rate, μ of 0.1 (10%), we see a change in

CH_4 mixing ratio from $\approx$0.001 mol/mol for a low burial fraction down to $\approx$0.0004 mol/mol when all organic carbon is buried (Figure 13a), with the CH_4 mixing ratio only dropping noticeably below 0.001 mol/mol when the burial fraction is greater than 0.1. This relatively small change is due to the fact that CH_4 is produced via catabolic reactions for 90% of the H_2 or CO that is consumed, while the burial fraction affects what happens to just the remaining 10%. This is further demonstrated in Equation 18, if $x = 1$ and $\mu = 0.1$, the methane flux will still come from 90% of the NPP. Adjusting the burial rate can thus only change the methane flux to be 90-100% of the NPP for this low growth rate case. Increasing the burial rate also has the effect of decreasing the biospheres productivity, shown in Figure 13b. This is because as the organic carbon burial fraction increases, less CH_4 is returning to the atmosphere, and thus less CH_4
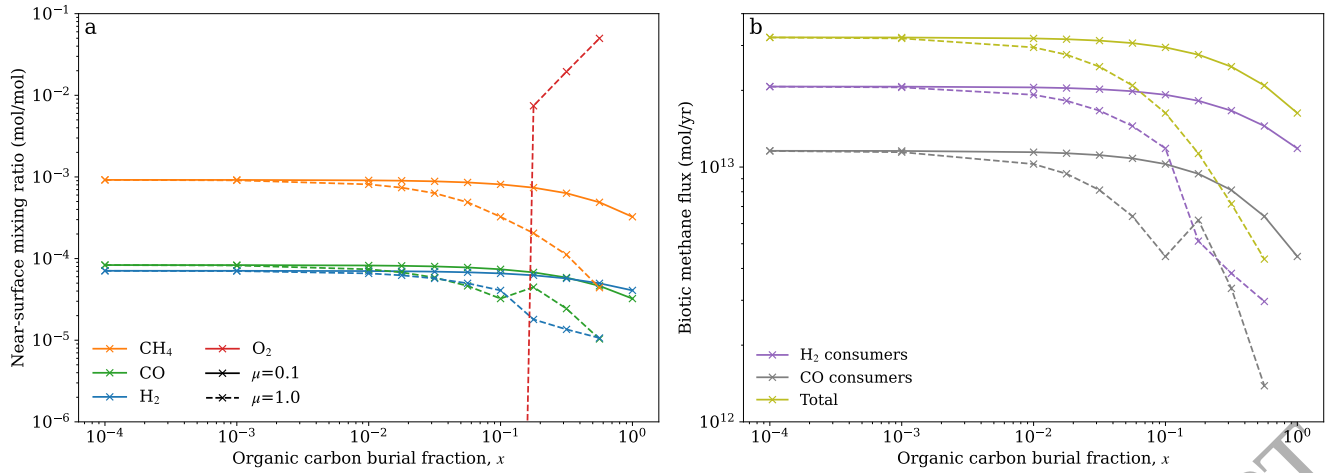
Figure 13. Comparison of the effects of H_2 organic carbon burial rates and growth efficiencies for a H_2 and CO consuming biosphere. (a) shows the change in near-surface composition vs burial fraction for H_2, CH_4, CO and O_2, while (b) shows the change in biosphere productivity of H_2 and CO consuming organisms. $\mu = 1.0$ (solid lines) represent a growth rate equivalent to a phototrophic primary production, while the lower growth rate of $\mu = 0.1$ (dashed lines) represents a biosphere that produces energy from catabolic reactions instead of using light.
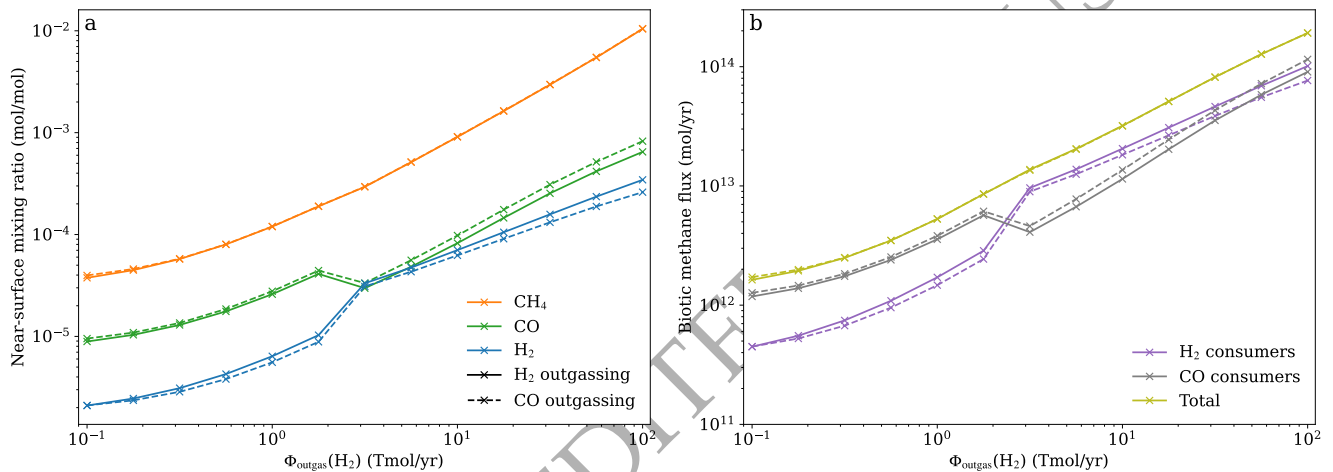
Figure 14. The effects of H_2 outgassing (solid lines) with an equivalent CO outgassing. (a) shows the change in near-surface (250 m above the surface) composition vs the outgassing rate for H_2, CH_4 and CO, while (b) shows the productivity of H_2 and CO consuming organisms.

is recycled back to H_2 and CO, where it can be consumed by the biosphere again.

In contrast to this, ecosystems with high growth rates, such as via anoxygenic photosynthesis are more sensitive to the organic carbon burial fraction. At low organic carbon burial fractions ($\lesssim 0.01$), the atmospheric composition is indistinguishable between low and high growth rates, which was also found in Earth like configurations (Kharecha et al. 2005). As the organic carbon burial fraction continues to decrease beyond 0.01, atmospheric CH_4 drops faster than the low growth rate case. This is because when the growth rate is higher, CH_4 is produced entirely by secondary consumers, rather than through catabolism processes, and the burial rate effectively determines how efficient secondary consumers are at recycling biomass. Again, by looking at Equation 18, and this time setting $\mu = 1$, now the methane flux can vary from 0 to 100 % of the NPP depending

on the burial rate, and the system is much more sensitive to this parameter when the growth rate is high. Thus, efficient recycling of organic carbon by secondary organisms is required to produce CH_4 levels that are distinguishable from abiotic configurations (compare Figure 13a to Figure 4).

For photosynthetic anoxic biospheres, if the organic carbon burial fraction is high, high O_2 scenarios become more likely. For $\Phi_{\text{outgas}}(H_2) = 10$ Tmol/yr, a burial fraction of greater than 0.1, can lead to high O_2 states. This is because of the large burial of reductant material and the significantly lower reducing power of the atmosphere from the low CH_4 production, alongside a H_2 consumption from the biosphere.
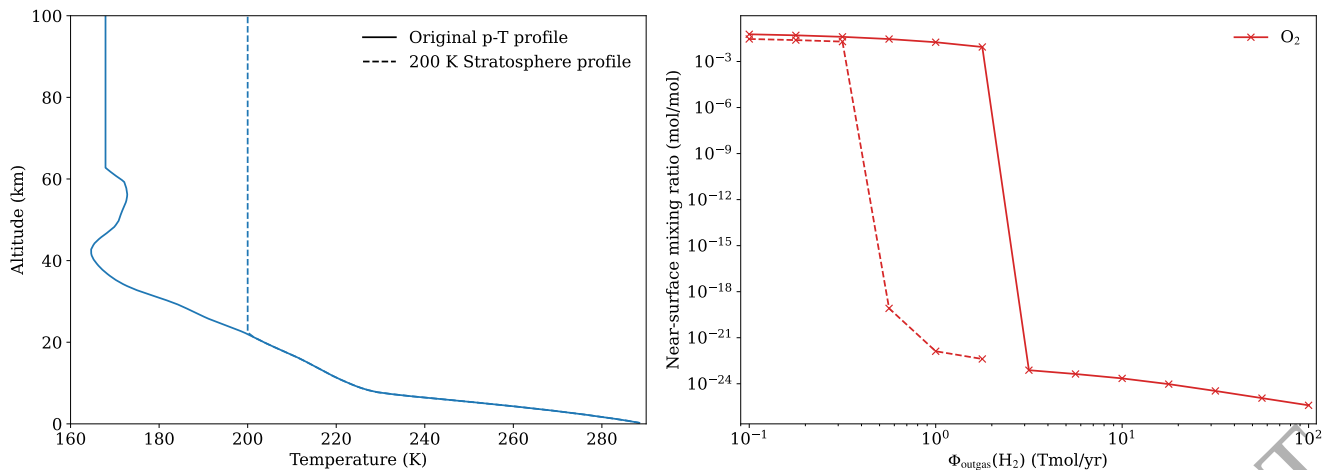
Figure 15. The effect of adjusting stratospheric temperature manually to a minimum of 200 K (a) on the near surface O_2 mixing ratio (b). Solid lines show the original temperature profile, while the dashed lines show results from the adjusted profile

5.3.4 Carbon monoxide outgassing

As volcanic input can vary depending on the carbon-to-hydrogen ratio in the mantle, we test the sensitivity of the atmosphere to CO and H_2 outgassing. Instead of volcanic flux from H_2, this is replaced with an equivalent CO flux, which is found to have a minor effect on the atmospheric composition. Figure 14a shows the near-surface mixing ratios from the key components of the atmosphere. Generally the atmospheric composition is the same for a given CO or H_2 flux, particularly for CH_4, while H_2 and CO are similar, apart from at higher volcanic outgassing fluxes where small differences emerge. Figure 14b shows the biotic CH_4 flux associated with these different outgassed gases, which generally show the same trend for both CO and H_2 consumers, with H_2 consumer productivity marginally higher when H_2 is outgassed compared to CO, and vice versa for CO consumer productivity.

5.3.5 Stratospheric temperature

The result of high oxygen mixing ratios under low reductant input caused by a CO consuming biosphere is sensitive to the stratospheric temperature. A warmer stratosphere (for example by setting the minimum stratospheric temperature to 200 K in Figure 15a) leads to an increase in the stratospheric water vapour content and thus increases the rate of stratospheric water vapour photolysis. This can then increase the rate of recombination of CO and O, which leads to the reductant limit on O_2 accumulation to occur at a lower reductant input, shown in Figure 15b.

5.4 Detectability of pre-photosynthetic biospheres on TRAPPIST-1e

Finally, we consider the detectability of potential preoxygenic-photosynthesising biospheres for a planet like TRAPPIST-1e. Abiotic and biotic configurations are now presented from PSG.

Biologically produced CH_4 shows strong signatures at high reductant input, but at low reductant input both the CH_4 and O_2/O_3 signatures are weak. The transmission spectra for abiotic, and biotic ecosystem 1 and 2 configurations are shown in Figure 16 for a range of

$\Phi_{outgas}(H_2)$. Both CO and CO_2 show strong features across all transmission spectra, while CH_4 shows obvious signals only for the biotic configurations, which are most visible at $\Phi_{outgas}(H_2)$ =100 Tmol/yr. Thus planets may need to have high outgassing rates for these biospheres to be detectable. The strongest O_3 feature is masked by CO_2 at 9.4 microns, although is most visible for ecosystem 1 when the reductant input is lowest. The inclusion of oxic metabolisms leads to this ozone feature being very difficult to distinguish from CO_2.

Although a CH_4 feature is present in our model transmission spectrum it is unlikely to be detectable through observations using the JWST. Figure 17 shows the synthetic spectra for NIRSpec PRISM in the 0.8-5.1 μm range for 20 transits (an effective upper limit) using PandExo (Batalha et al. 2017). Figure 17 shows that the CH_4 features would not be robustly detected at 1.2, 1.4 and 3.3 μm. CO_2 at 2.7 μm has the best change of detection, while CO at 2.3 μm could provide the best possibility for observation of this species. Beyond 5 μm, using MIRI, there are no chances of detection in this range (not shown). Therefore, detection of these signatures might require next generation observational facilities such as the ELT.

6 DISCUSSION

From our simulations, biospheres that consume H_2 and CO producing CH_4 as a waste product have the potential to be observed. Although detection of these may not be possible with JWST, future telescopes such as the ELT are likely to provide better opportunities for biosignature detection. Further, these results were specifically for TRAPPIST-1e, and other M-dwarf orbiting planets may prove to be better targets for observation. Signatures for CH_4 are present when the reductant input is greater than 10 Tmol/yr, which were absent in abiotic cases (see Figure 16). As well as this, strong features of CO_2 as well as signs of water vapour are seen in all cases. This could be sufficient to suggest a biosphere with Krissansen-Totton et al. (2018a) finding that this mix could provide a chemical disequilibrium strong enough to suggest the presence of life. However, strong CO features in transmission spectra, despite the presence of CO consuming organisms, may lead to some ambiguity as to whether this would be a definitively indicative biosphere (Thompson et al. 2022), despite
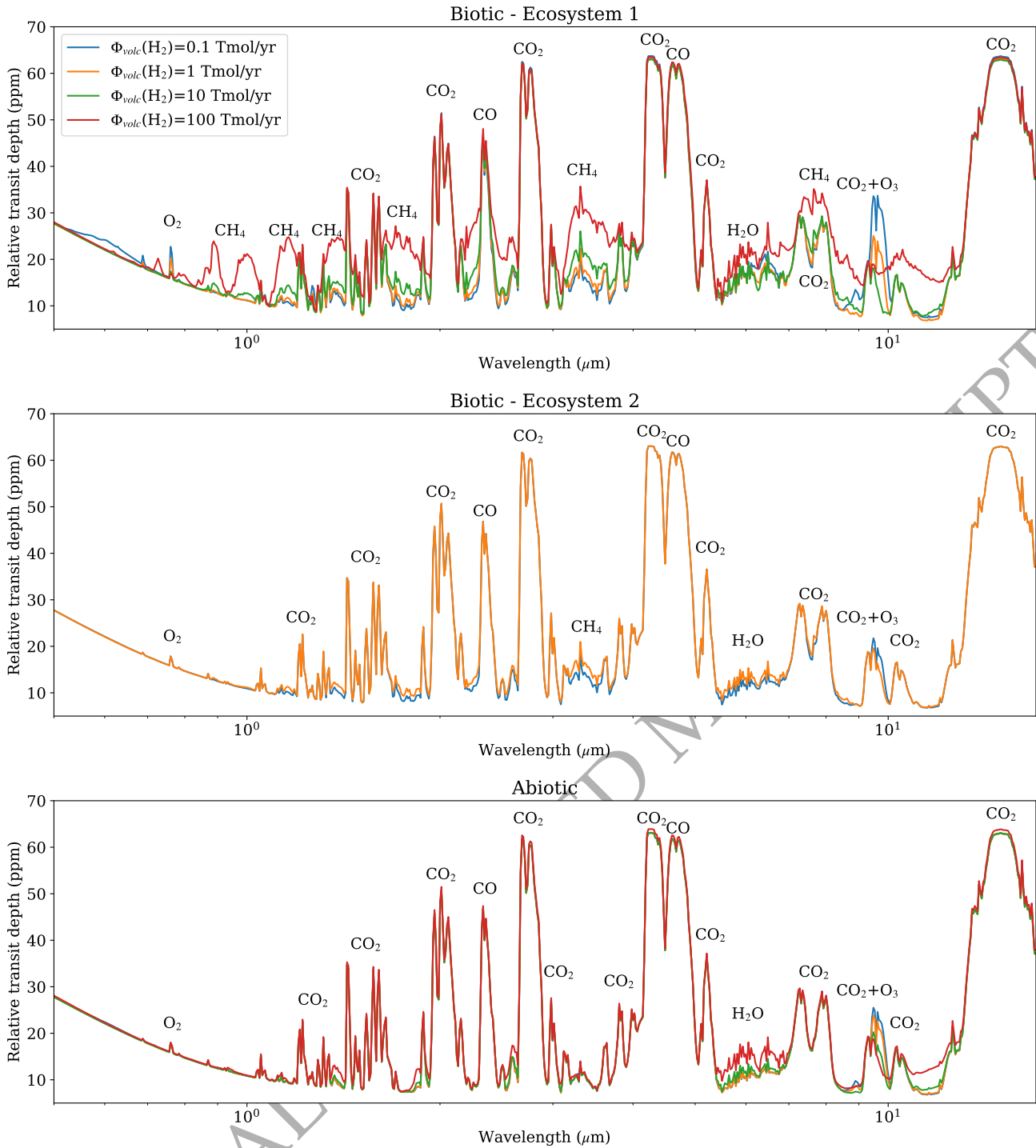
Figure 16. Transmission spectra for biotic and abiotic configurations used here for TRAPPIST-1e with stellar spectra that is quiescent and a mean flaring spectra. Transmission spectra is generated using PSG Villanueva et al. (2018), with features labelled with the species causing them.

near-surface concentrations of CO being orders of magnitude smaller than CH_4 (see Figure 6a). Our results do support the conclusions from Schwieterman et al. (2019) that CO does not necessarily represent an anti-biosignature and can accumulate to high concentrations on inhabited planets, particularly for M–dwarf orbiting planets.

As our transmission spectra is generated using a 1D model only,

without treatments of clouds and hazes, the effects of these have not been considered in the detectability. The presence of cloud may affect transmission spectra as discussed in Fauchez et al. (2019), which may mask some features around 20ppm. This may mean that if TRAPPIST-1e had a lower reductant input, the detection of CH_4 may not be possible, while a flux of greater than 1 Tmol/yr would
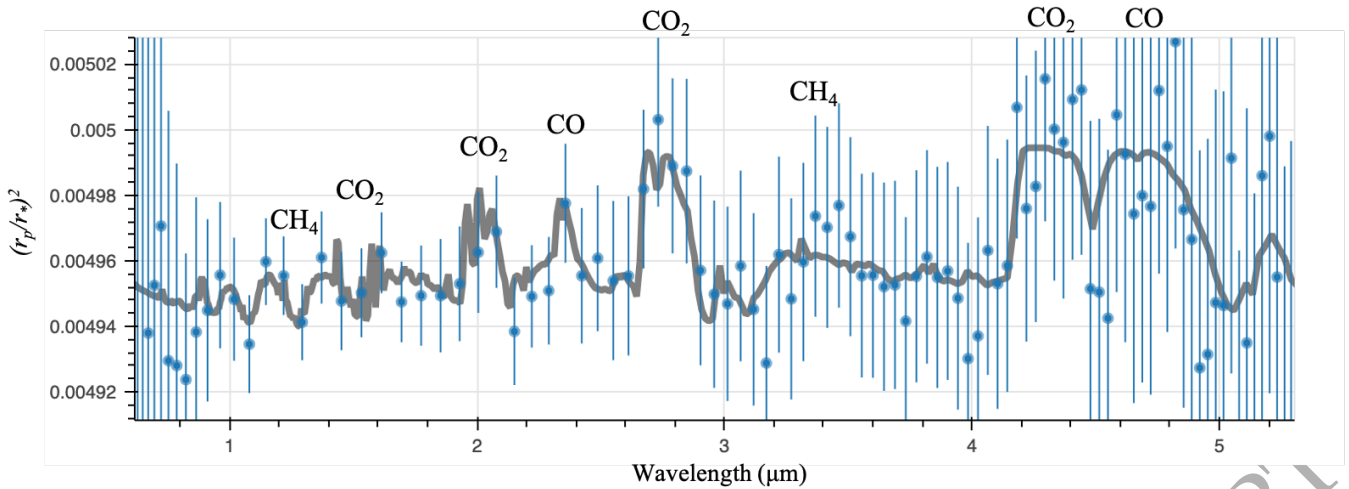
Figure 17. Synthetic observations generated using PandExo (Batalha et al. 2017) of TRAPPIST-1e with Ecosystem 1 and $\Phi_{outgas}(H_2)=100\,\mathrm{Tmol/yr}$. The observations are for NIRSpec with the Prism mode assume 20 transits, with four pixel bins. The transmission spectra used to generate the synthetic observations come from the PSG simulations presented in Figure 16. Visualisation of the data comes from https://exoctk.stsci.edu/pandexo/.

provide stronger signals. Similarly, a thin haze layer may be present in the highest H2 outgassing rate, which may clear many features below $3\,\mu m$ (Fauchez et al. 2019). However features of CH_4 beyond $3\,\mu m$ may be detectable, but only when H_2 outgassing is high, $\Phi_{outgas}(H_2) > 10\,\mathrm{Tmol/yr}$. We also find weaker CH_4 peaks compared to Fauchez et al. (2019). This may be because we find that CH_4 photolysis peaks deeper in the atmosphere, meaning CH_4 drops off substantially from around 50 km compared to above 80 km in Fauchez et al. (2019).

Segura et al. (2005) predicted that CH_4 concentrations would be higher if the biological CH_4 flux was the same as on Earth due to a lower rate of photochemical destruction. In addition to this, we find that the biological CH_4 flux is generally lower on TRAPPIST-1e compared with the Earth due to the difference in stellar spectrum. TRAPPIST-1 has a lower proportion of flux in the NUV, which leads to a lower rate of H_2O photolysis which reduces the amount of tropospheric OH. This is the predominant pathway for CH_4 destruction below approximately 50 km. The lower photochemical destruction of CH_4 reduces the rate at which CO and H_2 are produced and leads to a lower biological methane flux, when the H_2 outgassing is less than 10 Tmol/yr. As a result we find that CH_4 has a similar mixing ratio for both Earth and TRAPPIST-1e, with TRAPPIST-1e having only up to two times more CH_4. This difference is largest at a low reductant input, when there are high mixing ratios of oxygen, where the CH_4 lifetime is increased further as the production of the OH radical from H_2O photolysis is suppressed by an ozone layer.

Flaring has the potential to prevent the O_2 build up found at low $\Phi_{outgas}(H_2)$ in the quiescent state by increasing the UV flux. We provide a preliminary exploration of this using a mean flaring spectrum, shown in Figure 3, with the near-surface mixing ratios for key gases shown in Figure 18. The change in spectrum due to flaring could be sufficient to prevent O_2 accumulating to values of greater than 1%, seen in the quiescent state. The increased FUV flux due to flaring prevents O_2 and importantly O_3 accumulation, which maintains a weakly reducing atmosphere. This is by no means a comprehensive study of the effect of flaring, which would require time dependent modelling of atmospheric chemistry (e.g. Wogan et al. 2022; Ridg-
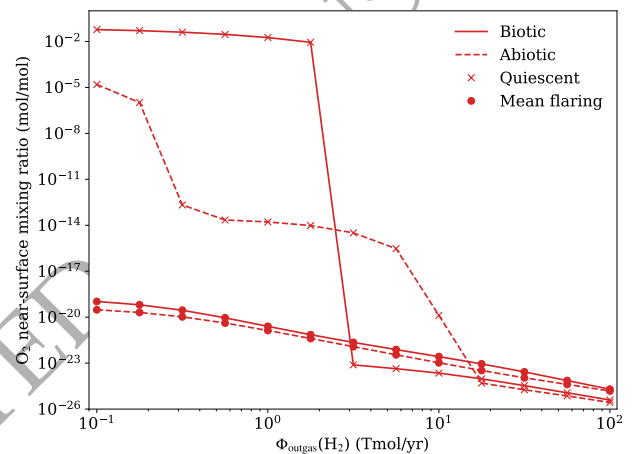
Figure 18. Near-surface (250 m above the surface) O_2 mixing ratio, for biotic and abiotic configurations for a quiescent and mean flaring spectrum of TRAPPIST-1.

way et al. 2022), but does provide a motivation for further work on the effects of flares.

An accurate vertical temperature profile is important to assess the potential for O_2 accumulation. For M-dwarfs, the stratospheric temperature is sensitive to the CO_2 and CH_4 mixing ratio, due to the high proportion of infrared stellar radiation, with stratospheric temperatures of 190-250 K plausible for TRAPPIST-1e (Mak et al. 2024). This can greatly affect the likelihood of atmospheric oxygen accumulation, and thus it is important to use temperature profiles that are more realistic for the atmospheric composition. This can be achieved through coupled climate chemistry models or using general circulation output in 1D chemistry models. The formation of ozone is unlikely to have a significant effect on the stratospheric temperature, as the ozone heating rate is much smaller for an M-dwarf spectrum (Boutle et al. 2017; Yates et al. 2020; Kozakis et al. 2022). This means

it is unlikely that O_3 formation could warm the stratosphere enough to then remove the ozone and produce either a stabilising negative feedback or an oscillating behaviour between a high and low ozone state. However, this could be investigated further in a coupled model.

The generation of high O_2 states by anoxygenic biospheres is likely to be affected by the CO_2 concentration. While we use a relatively low CO_2 abundance of 10%, higher CO_2 levels could see high levels of O_2 persisting for higher reductant inputs.

The oxidising regime that emerges at these low H_2 input levels in ecosystem 1, with only anoxic H_2 and CO consumers may also be missing important processes. At these levels of 10%, processes such as oxidative weathering are likely to be important (Daines et al. 2017). More work is required to establish the plausibility of the states with high O_2 levels found here due to different surface compositions.

The configuration used here effectively assumes a well-mixed rapidly-rotating planet. These planets are likely to be tidally-locked however, and either increasing the spatial resolution of 1D photochemical models to include day, night and terminator regions with appropriate mixing parametrisations or coupled chemistry-GCM are required to better constrain the detectability of these biospheres.

7 CONCLUSION

We use a coupled biosphere-atmosphere model to investigate the potential biosignatures from an H_2- and CO-consuming biosphere, which produces CH_4 as a waste product. We find that TRAPPIST-1e under a low reductant input with a CH_4 producing biosphere may produce relatively high levels of near-surface O_2 around 0.01–0.05 mol/mol, which is not seen in the Earth case. This is primarily due to the consumption of CO removing the major pathway for oxygen destruction in the atmosphere. In this high O_2 scenario, O_3 may be detectable at 9.4 microns, although this is difficult due to the presence of CO_2. The inclusion of O_2 consuming organisms, could reduce these O_2 levels to around 10^{-5} mol/mol. At higher reductant inputs, oxygen abundance decreases and strong features of CH_4 along with CO_2 may provide a robust biosignature. We also show that CO is likely to be present in high quantities, even with CO consuming organisms. The use of a mean flaring profile removes the high O_2 states shown, however further work is required to understand how a time-dependent flaring spectrum may affect the results observed. We have shown that anoxygenic photosynthesisers are unlikely to affect the atmospheric composition significantly compared to a methanogenic biosphere, unless the recycling efficiency of secondary producers is low, where atmospheric CH_4 becomes very low. These results show that simple biosphere models with consistent ocean fluxes are important in determining atmospheric composition for understanding the potential role of life on the atmospheric composition of exoplanets. The high oxygen state is sensitive to factors such as stratospheric temperature and thus further work using a coupled climate chemistry model are important for planets orbiting M-dwarfs.

DATA AVAILABILITY

The model output used for this study is available at doi.org/10.5281/zenodo.11002784.

REFERENCES

Adachi H., Basco N., James D. G. L., 1981, International Journal of Chemical Kinetics, 13, 1251

Agol E., et al., 2021, The Planetary Science Journal, 2, 1

Arthur M. A., Dean W. E., Neff E. D., Hay B. J., King J., Jones G., 1994, Global Biogeochemical Cycles, 8, 195

Babikov D., Semenov A., Teplukhin A., 2017, Geochimica et Cosmochimica Acta, 204, 388

Baggott J. E., Frey H. M., Lightfoot P. D., Walsh R., 1987, The Journal of Physical Chemistry, 91, 3386

Basco N., Pearson A. E., 1967, Transactions of the Faraday Society, 63, 2684

Batalha N. E., et al., 2017, Publications of the Astronomical Society of the Pacific, 129, 064501

Battistuzzi F. U., Feijao A., Hedges S. B., 2004, BMC Evolutionary Biology, 4, 44

Baulch D. L., et al., 1992, Journal of Physical and Chemical Reference Data, 21, 411

Baulch D. L., et al., 1994, Journal of Physical and Chemical Reference Data, 23, 847

Baulch D. L., et al., 2005, Journal of Physical and Chemical Reference Data, 34, 757

Berner R. A., 1982, American Journal of Science, 282, 451

Boutle I. A., Mayne N. J., Drummond B., Manners J., Goyal J., Hugo Lambert F., Acreman D. M., Earnshaw P. D., 2017, Astronomy & Astrophysics, 601, A120

Brune W. H., Schwab J. J., Anderson J. G., 1983, The Journal of Physical Chemistry, 87, 4503

Burkholder J. B., et al., 2015, Technical report, "Chemical Kinetics and Photochemical Data for Use in Atmospheric Studies, Evaluation No. 18," JPL Publication 15-10, http://jpldataeval.jpl.nasa.gov. Jet Propulsion Laboratory, Pasadena, http://jpldataeval.jpl.nasa.gov

Burkholder J. B., et al., 2019, Technical report, Chemical Kinetics and Photochemical Data for Use in Atmospheric Studies, Evaluation No. 19,. Jet Propulsion Laboratory, Pasadena

Campbell I., Gray C., 1973, Chemical Physics Letters, 18, 607
Canosa-mas C. E., Frey H. M., Walsh R., 1984, J. Chem. Soc., Faraday Trans. 2, 80, 561
Catling D. C., et al., 2018, Astrobiology, 18, 709
Chen H., Zhan Z., Youngblood A., Wolf E. T., Feinstein A. D., Horton D. E., 2020, Nature Astronomy, 5, 298
Choi Y. M., Lin M. C., 2005, International Journal of Chemical Kinetics, 37, 261
Chung K., Calvert J. G., Bottenheim J. W., 1975, International Journal of Chemical Kinetics, 7, 161
Claire M. W., Sheets J., Cohen M., Ribas I., Meadows V. S., Catling D. C., 2012, The Astrophysical Journal, 757, 95
Daines S. J., Lenton T. M., 2016, Earth and Planetary Science Letters, 434, 42
Daines S. J., Mills B. J. W., Lenton T. M., 2017, Nature Communications, 8, 14379
Dammeier J., Colberg M., Friedrichs G., 2007, Physical Chemistry Chemical Physics, 9, 4177
Davidson J. A., Schiff H. I., Brown T. J., Howard C. J., 1978, The Journal of Chemical Physics, 69, 1216
Davies H. S., Duarte J. C., Green M., 2023, in , A Journey Through Tides. Elsevier, pp 133–141, doi:10.1016/B978-0-323-90851-1.00020-0
Devriendt K., Peeters J., 1997, The Journal of Physical Chemistry A, 101, 2546
Dillon T. J., Horowitz A., Crowley J. N., 2007, Chemical Physics Letters, 443, 12
Domagal-Goldman S. D., Meadows V. S., Claire M. W., Kasting J. F., 2011, Astrobiology, 11, 419
Domagal-Goldman S. D., Segura A., Claire M. W., Robinson T. D., Meadows V. S., 2014, The Astrophysical Journal, 792, 90
Du S., Francisco J. S., Shepler B. C., Peterson K. A., 2008, The Journal of Chemical Physics, 128
Du S., Germann T. C., Francisco J. S., Peterson K. A., Yu H.-G., Lyons J. R., 2011, The Journal of Chemical Physics, 134
Eager-Nash J. K., et al., 2020, Astronomy & Astrophysics, 639, A99
Eager-Nash J. K., et al., 2023, Journal of Geophysical Research: Atmospheres, 128
Edwards J. M., Slingo A., 1996, Quarterly Journal of the Royal Meteorological Society, 122, 689
Fardeau M.-L., Belaich J.-P., 1986, Archives of Microbiology, 144, 381
Fauchez T. J., et al., 2019, The Astrophysical Journal, 887, 194
Fauchez T., et al., 2020, Geosci. Model Dev., 13, 707
Ferry J. G., 2006, Molecular Biology and Evolution, 23, 1286
Gao Y., Marshall P., 2011, The Journal of Chemical Physics, 135
Gauthier M. J., Snelling D. R., 1975, Journal of Photochemistry, 4, 27
Gillon M., et al., 2017, Nature, 542, 456
Giorgi F., Chameides W. L., 1985, Journal of Geophysical Research: Atmospheres, 90, 7872
Gladstone G., Allen M., Yung Y., 1996, Icarus, 119, 1
Gough D. O., 1981, Solar Physics, 74, 21
Greene T. P., Bell T. J., Ducrot E., Dyrek A., Lagage P.-O., Fortney J. J., 2023, Nature, 618, 39
Gregory B. S., Claire M. W., Rugheimer S., 2021, Earth and Planetary Science Letters, 561, 116818
Guimond C. M., Noack L., Ortenzi G., Sohl F., 2021, Physics of the Earth and Planetary Interiors, 320, 106788
Harman C. E., Schwieterman E. W., Schottelkotte J. C., Kasting J. F., 2015, The Astrophysical Journal, 812, 137
Harman C. E., Felton R., Hu R., Domagal-Goldman S. D., Segura A., Tian F., Kasting J. F., 2018, The Astrophysical Journal, 866, 56
Harris L. B., Bédard J. H., 2014, Springer, Dordrecht, pp 215–291, doi:10.1007/978-94-007-7615-9_9
Hassinen E., Kalliorinne K., Koskikallio J., 1990, International Journal of Chemical Kinetics, 22, 741
Hawley S. L., Davenport J. R. A., Kowalski A. F., Wisniewski J. P., Hebb L., Deitrick R., Hilton E. J., 2014, The Astrophysical Journal, 797, 121
Herron J. T., 1988, Journal of Physical and Chemical Reference Data, 17, 967
Hu R., Seager S., Bains W., 2012, The Astrophysical Journal, 761, 166

Hu R., Peterson L., Wolf E. T., 2020, The Astrophysical Journal, 888, 122
Ih J., Kempton E. M.-R., Whittaker E. A., Lessard M., 2023, The Astrophysical Journal Letters, 952, L4
Karman T., et al., 2019, Icarus, 328, 160
Kasting J. F., 1990, Origins of Life and Evolution of the Biosphere, 20, 199
Kasting J. F., Eggler D. H., Raeburn S. P., 1993, The Journal of Geology, 101, 245
Kasting J. F., Pavlov A. A., Siefert J. L., 2001, Origins of Life and Evolution of the Biosphere, 31, 271
Kharecha P., Kasting J., Siefert J., 2005, Geobiology, 3, 53
Knoll A. H., Nowak M. A., 2017, Science Advances, 3
Korenaga J., 2013, Annual Review of Earth and Planetary Sciences, 41, 117
Kozakis T., Mendonça J. M., Buchhave L. A., 2022, Astronomy & Astrophysics, 665, A156
Krasnoperov L., Chesnokov E., Stark H., Ravishankara A., 2005, Proceedings of the Combustion Institute, 30, 935
Krasnopolsky V. A., 2012, Icarus, 218, 230
Krissansen-Totton J., Olson S., Catling D. C., 2018a, Science Advances, 4
Krissansen-Totton J., Garland R., Irwin P., Catling D. C., 2018b, The Astronomical Journal, 156, 114
Kurbanov M. A., Mamedov K. F., 1995, Kinetics and Catalysis, 36
Langford R. B., Oldershaw G. A., 1972, Journal of the Chemical Society, Faraday Transactions 1: Physical Chemistry in Condensed Phases, 68, 1550
Lee J. H., Stief L. J., Timmons R. B., 1977, The Journal of Chemical Physics, 67, 1705
Lenton T., Watson A., 2011, Revolutions that made the Earth. Oxford University Press, doi:10.1093/acprof:oso/9780199587049.001.0001
Lessner D. J., et al., 2006, Proceedings of the National Academy of Sciences, 103, 17921
Lichtin D., Berman M., Lin M., 1984, Chemical Physics Letters, 108, 18
Lincowski A. P., Meadows V. S., Crisp D., Robinson T. D., Luger R., Lustig-Yaeger J., Arney G. N., 2018, The Astrophysical Journal, 867, 76
Lincowski A. P., et al., 2023, The Astrophysical Journal Letters
Liss P. S., Slater P. G., 1974, Nature, 247, 181
Loison J.-C., Halvick P., Bergeat A., Hickson K. M., Wakelam V., 2012, Monthly Notices of the Royal Astronomical Society, 421, 1476
Lourenço D. L., Rozel A. B., 2023, in , Dynamics of Plate Tectonics and Mantle Convection. Elsevier, pp 181–196, doi:10.1016/B978-0-323-85733-8.00004-4
Lourenço D. L., Rozel A. B., Ballmer M. D., Tackley P. J., 2020, Geochemistry, Geophysics, Geosystems, 21
Lu C.-W., Wu Y.-J., Lee Y.-P., Zhu R. S., Lin M. C., 2006, The Journal of Chemical Physics, 125
Luger R., Barnes R., 2015, Astrobiology, 15, 119
Mak M. T., et al., 2024, Monthly Notices of the Royal Astronomical Society, 529, 3971
Manabe S., Strickler R. F., 1964, Journal of the Atmospheric Sciences, 21, 361
Manabe S., Wetherald R. T., 1967, Journal of the Atmospheric Sciences, 24, 241
Manners J., Edwards J. M., Hill P., Thelen J.-C., 2022, SOCRATES (Suite Of Community RAdiative Transfer codes based on Edwards and Slingo) Technical Guide
Martinez R. I., Herron J. T., 1983, International Journal of Chemical Kinetics, 15, 1127
McCollom T. M., Bach W., 2009, Geochimica et Cosmochimica Acta, 73, 856
Meadows V. S., et al., 2018, Astrobiology, 18, 133
Morii H., Koga Y., Nagai S., 1987, Biotechnology and Bioengineering, 29, 310
Nicholas J. E., Amodio C. A., Baker M. J., 1979, Journal of the Chemical Society, Faraday Transactions 1: Physical Chemistry in Condensed Phases, 75, 1868
Nicholson A. E., Daines S. J., Mayne N. J., Eager-Nash J. K., Lenton T. M., Kohary K., 2022, Monthly Notices of the Royal Astronomical Society, 517, 222
Olson S. L., Jansen M., Abbot D. S., 2020, The Astrophysical Journal, 895,

19

Ozaki K., Tajika E., Hong P. K., Nakagawa Y., Reinhard C. T., 2018, Nature Geoscience, 11, 55

Palin R. M., Santosh M., 2021, Gondwana Research, 100, 3

Peacock S., Barman T., Shkolnik E. L., Hauschildt P. H., Baron E., 2019, The Astrophysical Journal, 871, 235

Peng J., Hu X., Marshall P., 1999, The Journal of Physical Chemistry A, 103, 5307

Pinto J. P., Gladstone G. R., Yung Y. L., 1980, Science, 210, 183

Ranjan S., Schwieterman E. W., Harman C., Fateev A., Sousa-Silva C., Seager S., Hu R., 2020, The Astrophysical Journal, 896, 148

Ranjan S., Schwieterman E. W., Leung M., Harman C. E., Hu R., 2023, Submitted to AAS Journals

Ridgway R. J., et al., 2022, Monthly Notices of the Royal Astronomical Society, 518, 2472

Rosing M. T., 1999, Science, 283, 674

Rothman L. S., et al., 2013, Journal of Quantitative Spectroscopy and Radiative Transfer, 130, 4

Rugheimer S., Kaltenegger L., 2018, The Astrophysical Journal, 854, 19

Rugheimer S., Kaltenegger L., Segura A., Linsky J., Mohanty S., 2015, The Astrophysical Journal, 809, 57

Salazar A. M., Olson S. L., Komacek T. D., Stephens H., Abbot D. S., 2020, The Astrophysical Journal, 896

Sauterey B., Charnay B., Affholder A., Mazevet S., Ferrière R., 2020, Nature Communications, 11, 2705

Schofield K., 1973, Journal of Physical and Chemical Reference Data, 2, 25

Schonheit P., Moll J., Thauer R. K., 1980, Archives of Microbiology, 127, 59

Schwieterman E. W., Reinhard C. T., Olson S. L., Ozaki K., Harman C. E., Hong P. K., Lyons T. W., 2019, The Astrophysical Journal, 874, 9

Segura A., Kasting J. F., Meadows V., Cohen M., Scalo J., Crisp D., Butler R. A., Tinetti G., 2005, Astrobiology, 5, 706

Shields A. L., Meadows V. S., Bitz C. M., Pierrehumbert R. T., Joshi M. M., Robinson T. D., 2013, Astrobiology, 13, 715

Singleton D. L., Cvetanović R. J., 1988, Journal of Physical and Chemical Reference Data, 17, 1377

Slanger T. G., Wood B. J., Black G., 1972, The Journal of Chemical Physics, 57, 233

Solomatov V. S., 1995, Physics of Fluids, 7, 266

Stachnik R. A., Molina M. J., 1987, The Journal of Physical Chemistry, 91, 4603

Teal D. J., Kempton E. M.-R., Bastelberger S., Youngblood A., Arney G., 2022, The Astrophysical Journal, 927, 90

Thiesemann H., MacNamara J., Taatjes C. A., 1997, The Journal of Physical Chemistry A, 101, 1881

Thompson M. A., Krissansen-Totton J., Wogan N., Telus M., Fortney J. J., 2022, Proceedings of the National Academy of Sciences, 119

Tian F., France K., Linsky J. L., Mauas P. J., Vieytes M. C., 2014, Earth and Planetary Science Letters, 385, 22

Tiee J., Wampler F., Oldenborg R., Rice W., 1981, Chemical Physics Letters, 82, 80

Toon O. B., Kasting J. F., Turco R. P., Liu M. S., 1987, Journal of Geophysical Research, 92, 943

Tsang W., Hampson R. F., 1986, Journal of Physical and Chemical Reference Data, 15, 1087

Tsang W., Herron J. T., 1991, Journal of Physical and Chemical Reference Data, 20, 609

Turbet M., Boulet C., Karman T., 2020, Icarus, 346, 113762

Turco R. P., Whitten R. C., Toon O. B., 1982, Reviews of Geophysics, 20, 233

Villanueva G., Smith M., Protopapa S., Faggi S., Mandell A., 2018, Journal of Quantitative Spectroscopy and Radiative Transfer, 217, 86

Walker J. C. G., Hays P. B., Kasting J. F., 1981, Journal of Geophysical Research, 86, 9776

Ward L. M., Rasmussen B., Fischer W. W., 2019, Journal of Geophysical Research: Biogeosciences, 124, 211

Watson A. J., 2008, Astrobiology, 8, 175

Weiss M. C., Sousa F. L., Mrnjavac N., Neukirchen S., Roettger M., Nelson-Sathi S., Martin W. F., 2016, Nature Microbiology, 1, 16116

Wilson D. J., et al., 2021, The Astrophysical Journal, 911, 18

Wine P. H., Chameides W. L., Ravishankara A. R., 1981, Geophysical Research Letters, 8, 543

Wogan N. F., Catling D. C., Zahnle K. J., Claire M. W., 2022, Proceedings of the National Academy of Sciences, 119

Wunderlich F., et al., 2020, The Astrophysical Journal, 901, 126

Yates J. S., Palmer P. I., Manners J., Boutle I., Kohary K., Mayne N., Abraham L., 2020, Monthly Notices of the Royal Astronomical Society, 492

Yung Y. L., Demore W., 1982, Icarus, 51, 199

Yung Y. L., Allen M., Pinto J. P., 1984, The Astrophysical Journal Supplement Series, 55, 465

Zabarnick S., Fleming J. W., Lin M. C., 1989, International Journal of Chemical Kinetics, 21, 765

Zahnle K. J., 1986, Journal of Geophysical Research: Atmospheres, 91, 2819

Zahnle K., Claire M., Catling D., 2006, Geobiology, 4, 271

Zieba S., et al., 2023, Nature

APPENDIX A: PHOTOCHEMICAL MODEL

The Species list along with the deposition velocities employed here are in Table 1. Photolysis reactions are listed in Table A1. For bimolecular reactions the rate coefficient, k, is calculated from the Arrhenius equation

$$k = A \left(\frac{T}{300} \right)^{\alpha} e^{-\beta/T}, \tag{A1}$$

where A is a pre-exponential factor, T is temperature in kelvins, α determines the degree of the temperature dependence for the reaction, β is the divided by the gas constant. The parameters for each of the bimolecular reactions and their sources is listed in Table A2.

For termolecular reactions, the rate coefficient is

$$k = \frac{k_0 [M]}{1 + \frac{k_0}{k_\infty}[M]} F. \tag{A2}$$

where k_0 and k_∞ are the low and high-pressure limits of the rate coefficient respectively:

$$k_0 = A_1 \left(\frac{T}{300} \right)^{\alpha_1} e^{-\beta_1/T} \tag{A3}$$

$$k_\infty = A_2 \left(\frac{T}{300} \right)^{\alpha_2} e^{-\beta_2/T} \tag{A4}$$

with the terms for these mirroring those of Equation A1. F is a broadening factor, which takes the form

$$F = F_c^{\frac{1}{1+(\log P_r)^2}} \tag{A5}$$

where F_c is a parameter greater than zero or less than or equal to one, and P_r, known as the reduced pressure is

$$P_r = \frac{k_0}{k_\infty}[M]. \tag{A6}$$

The parameters for each of the termolecular reactions and their sources is listed in Table A3.

The Eddy diffusion coefficient used in this study is shown in Figure A1.

Table A1. Photolysis reactions used in this network, with reactants (R) and products (P), with cross section and quantum yields from the open access ATMOS model (Teal et al. 2022). The horizontal line within the table shows the cutoff for the CHO network.

R1	R2	P1	P2	P3
O_2	$h\nu$	$O(^3P)$	$O(^1D)$	-
O_2	$h\nu$	$O(^3P)$	$O(^3P)$	-
H_2O	$h\nu$	H	OH	-
H_2O	$h\nu$	H_2	$O(^1D)$	-
H_2O	$h\nu$	H	H	$O(^3P)$
O_3	$h\nu$	O_2	$O(^1D)$	-
O_3	$h\nu$	O_2	$O(^3P)$	-
H_2O_2	$h\nu$	OH	OH	-
H_2O_2	$h\nu$	H	HO_2	-
CO_2	$h\nu$	CO	$O(^3P)$	-
CO_2	$h\nu$	CO	$O(^1D)$	-
H_2CO	$h\nu$	H_2	CO	-
H_2CO	$h\nu$	HCO	H	-
HO_2	$h\nu$	OH	$O(^3P)$	-
HO_2	$h\nu$	OH	$O(^1D)$	-
CH_4	$h\nu$	$^1CH_2$	H_2	-
CH_4	$h\nu$	CH_3	H	-
CH_4	$h\nu$	$^3CH_2$	H	H
C_2H_6	$h\nu$	$^3CH_2$	$^3CH_2$	H_2
C_2H_6	$h\nu$	CH_4	$^1CH_2$	-
C_2H_6	$h\nu$	C_2H_2	H_2	H_2
C_2H_6	$h\nu$	C_2H_4	H	H
C_2H_6	$h\nu$	C_2H_4	H_2	-
C_2H_6	$h\nu$	CH_3	CH_3	-
CH	$h\nu$	C	H	-
CH_2CO	$h\nu$	$^3CH_2$	CO	-
C_2H_2	$h\nu$	C2H	H	-
C_2H_2	$h\nu$	C2	H_2	-
C_2H_4	$h\nu$	C_2H_2	H_2	-
C_2H_4	$h\nu$	C_2H_2	H	H
CH_3CHO	$h\nu$	CH_3	HCO	-
CH_3CHO	$h\nu$	CH_4	CO	-
HNO_2	$h\nu$	NO	OH	-
HNO_3	$h\nu$	NO_2	OH	-
NO	$h\nu$	N	$O(^3P)$	-
NO_2	$h\nu$	NO	$O(^3P)$	-
SO	$h\nu$	S	$O(^3P)$	-
H_2S	$h\nu$	HS	H	-
SO_2	$h\nu$	SO	$O(^3P)$	-
SO_2	$h\nu$	$^1SO_2$	-	-
SO_2	$h\nu$	$^3SO_2$	-	-
S_2	$h\nu$	S	S	-
S_4	$h\nu$	S_2	S_2	-
S_3	$h\nu$	S_2	S	-
SO_3	$h\nu$	SO_2	$O(^3P)$	-
HSO	$h\nu$	HS	$O(^3P)$	-
OCS	$h\nu$	CO	S	-
HO_2NO_2	$h\nu$	HO_2	NO_2	-
HO_2NO_2	$h\nu$	OH	NO_3	-
N_2O_5	$h\nu$	NO_3	NO_2	-
N_2O_5	$h\nu$	NO_3	NO	$O(^3P)$
NO_3	$h\nu$	NO	O_2	-
NO_3	$h\nu$	NO_2	$O(^3P)$	-
N_2O	$h\nu$	N_2	$O(^1D)$	-
CS_2	$h\nu$	CS	S	-
CS_2	$h\nu$	CS_2^*	-	-

Figure A1. Eddy diffusion coefficient profile used in this study.

Table A2: Bimolecular reactions used in this network. Reactions sourced from the Kinetic Database for Astrochemistry (KIDA) are from `https://kida.astrochem-tools.org/`. The horizontal line within the table shows the cut-off for the CHO network.

R1	R2	R3	P1	P2	P3	A	α	β (K)	Source
$O(^1D)$	H_2O	-	OH	OH	-	1.63e-10	0.000	-60	Burkholder et al. (2019)
$O(^1D)$	H_2	-	OH	H	-	1.20e-10	0.000	0	Burkholder et al. (2019)
H_2	$O(^3P)$	-	OH	H	-	3.44e-13	2.670	3160	Baulch et al. (1992)
OH	H_2	-	H_2O	H	-	2.80e-12	0.000	1800	Burkholder et al. (2019)
H	O_3	-	OH	O_2	-	1.40e-10	0.000	470	Burkholder et al. (2019)
H	HO_2	-	H_2	O_2	-	6.90e-12	0.000	0	Burkholder et al. (2019)
H	HO_2	-	$O(^3P)$	H_2O	-	1.60e-12	0.000	0	Burkholder et al. (2019)
H	HO_2	-	OH	OH	-	7.20e-11	0.000	0	Burkholder et al. (2019)
$O(^3P)$	OH	-	O_2	H	-	1.80e-11	0.000	-180	Burkholder et al. (2019)
OH	HO_2	-	H_2O	O_2	-	4.80e-11	0.000	-250	Burkholder et al. (2019)
OH	O_3	-	HO_2	O_2	-	1.70e-12	0.000	940	Burkholder et al. (2019)
$O(^3P)$	HO_2	-	OH	O_2	-	3.00e-11	0.000	-200	Burkholder et al. (2019)
HO_2	O_3	-	OH	O_2	O_2	1.00e-14	0.000	490	Burkholder et al. (2019)
HO_2	HO_2	-	H_2O_2	O_2	-	3.00e-13	0.000	-460	Burkholder et al. (2019)
OH	H_2O_2	-	H_2O	HO_2	-	1.80e-12	0.000	0	Burkholder et al. (2019)
$O(^3P)$	O_3	-	O_2	O_2	-	8.00e-12	0.000	2060	Burkholder et al. (2019)
OH	OH	-	H_2O	$O(^3P)$	-	1.80e-12	0.000	0	Burkholder et al. (2019)
$O(^1D)$	N_2	-	$O(^3P)$	N_2	-	2.15e-11	0.000	-110	Burkholder et al. (2019)
$O(^1D)$	O_2	-	$O(^3P)$	O_2	-	3.30e-11	0.000	-55	Burkholder et al. (2019)
OH	CO	-	H	CO_2	-	1.50e-13	0.000	0	Burkholder et al. (2015)
H	HCO	-	H_2	CO	-	1.83e-10	0.000	0	KIDA
HCO	HCO	-	H_2CO	CO	-	4.48e-11	0.000	0	KIDA
OH	HCO	-	H_2O	CO	-	1.80e-10	0.000	0	KIDA
$O(^3P)$	HCO	-	H	CO_2	-	5.00e-11	0.000	0	KIDA
$O(^3P)$	HCO	-	OH	CO	-	5.00e-11	0.000	0	KIDA
HCO	$h\nu$	-	H	CO	-	1.00e-02	0.000	0	Pinto et al. (1980)
H_2CO	H	-	H_2	HCO	-	2.16e-12	1.620	1090	KIDA
HCO	O_2	-	CO	HO_2	-	5.20e-12	0.000	0	Burkholder et al. (2015)
OH	H_2CO	-	H_2O	HCO	-	5.50e-12	0.000	-125	Burkholder et al. (2015)
H_2CO	$O(^3P)$	-	HCO	OH	-	3.40e-11	0.000	1600	Burkholder et al. (2015)
$O(^3P)$	H_2O_2	-	OH	HO_2	-	1.40e-12	0.000	2000	Burkholder et al. (2019)
OH	CH_4	-	CH_3	H_2O	-	2.45e-12	0.000	1775	Burkholder et al. (2015)
$O(^1D)$	CH_4	-	CH_3	OH	-	1.66e-10	0.000	0	Burkholder et al. (2015)
$O(^1D)$	CH_4	-	H_2CO	H_2	-	8.75e-12	0.000	0	Burkholder et al. (2015)
$^1CH_2$	CH_4	-	CH_3	CH_3	-	3.60e-11	0.000	0	Zahnle et al. (2006))
$^1CH_2$	O_2	-	H	CO	OH	2.05e-11	0.000	750	Baulch et al. (1994)
$^1CH_2$	O_2	-	H_2	CO_2	-	2.05e-11	0.000	750	Baulch et al. (1994)
$^1CH_2$	N_2	-	$^3CH_2$	N_2	-	1.00e-11	0.000	0	KIDA
$^3CH_2$	H_2	-	CH_3	H	-	5.00e-15	0.000	0	Tsang & Hampson (1986)
$^3CH_2$	CH_4	-	CH_3	CH_3	-	7.13e-12	0.000	5050	KIDA
$^3CH_2$	O_2	-	HCO	OH	-	4.10e-11	0.000	750	Zahnle et al. (2006)
CH_3	O_2	-	H_2CO	OH	-	3.00e-16	0.000	0	Burkholder et al. (2015)
CH_3	$O(^3P)$	-	H_2CO	H	-	1.10e-10	0.000	0	Burkholder et al. (2015)
CH_3	O_3	-	CH_3O	O_2	-	5.40e-12	0.000	220	Burkholder et al. (2015)
CH_3	OH	-	CH_3O	H	-	1.20e-12	0.000	2760	KIDA
CH_3	$h\nu$	-	$^3CH_2$	H	-	1.00e-05	0.000	0	Zahnle et al. (2006)
CH_3	HCO	-	CH_4	CO	-	9.30e-11	0.000	0	Krasnoperov et al. (2005)
CH_3	H_2CO	-	CH_4	HCO	-	1.12e-14	3.360	2170	KIDA
CH_4	$O(^3P)$	-	CH_3	OH	-	8.41e-12	1.560	4280	KIDA
$^1CH_2$	H_2	-	CH_3	H	-	1.20e-10	0.000	0	KIDA
$^1CH_2$	H_2	-	$^3CH_2$	H_2	-	1.26e-11	0.000	0	KIDA
$^1CH_2$	CO_2	-	H_2CO	CO	-	1.00e-12	0.000	0	Zahnle (1986)
$^3CH_2$	$O(^3P)$	-	CO	H	H	2.04e-10	0.000	270	KIDA

Continued on next page

Table A2 – continued from previous page

R1	R2	R3	P1	P2	P3	A	α	β (K)	Source
$^3CH_2$	CO_2	-	H_2CO	CO	-	3.90e-14	0.000	0	Tsang & Hampson (1986)
OH	C_2H_6	-	H_2O	C_2H_5	-	7.66e-12	0.000	1020	Burkholder et al. (2015)
C_2H_6	$O(^3P)$	-	C_2H_5	OH	-	8.63e-12	1.500	2920	KIDA
C_2H_6	$O(^1D)$	-	OH	C_2H_5	-	3.40e-11	0.000	0	Dillon et al. (2007)
C_2H_6	$O(^1D)$	-	H_2O	C_2H_4	-	1.02e-10	0.000	0	Dillon et al. (2007)
C_2H_6	$O(^1D)$	-	CH_3	CH_3O	-	2.04e-10	0.000	0	Dillon et al. (2007)
C_2H_5	HCO	-	C_2H_6	CO	-	7.21e-11	0.000	0	Baggott et al. (1987)
CO	$O(^1D)$	-	CO	$O(^3P)$	-	4.70e-11	0.000	-63	Davidson et al. (1978)
C_2H_5	H	-	CH_3	CH_3	-	6.00e-11	0.000	0	Baulch et al. (1992)
C_2H_5	$O(^3P)$	-	CH_3	HCO	H	3.00e-11	0.000	0	Tsang & Hampson (1986)
C_2H_5	OH	-	CH_3	HCO	H_2	4.00e-11	0.000	0	Zahnle et al. (2006)
CH_3O_2	H	-	CH_3O	OH	-	1.60e-10	0.000	0	Tsang & Hampson (1986)
CH_3O_2	$O(^3P)$	-	CH_3O	O_2	-	8.30e-11	0.000	0	Herron (1988)
HCO	$^3CH_2$	-	CH_3	CO	-	3.00e-11	0.000	0	Tsang & Hampson (1986)
CH_3O	CO	-	CH_3	CO_2	-	2.60e-11	0.000	5940	KIDA
$^3CH_2$	$O(^3P)$	-	CO	H_2	-	1.36e-10	0.000	270	KIDA
CH_3	OH	-	H_2CO	H_2	-	5.30e-15	0.000	2530	KIDA
C_2H_5	O_2	-	C_2H_4	HO_2	-	1.00e-14	0.000	0	Burkholder et al. (2015)
C_2H_5	H	-	C_2H_4	H_2	-	3.00e-12	0.000	0	KIDA
C_2H_5	$O(^3P)$	-	H_2CO	CH_3	-	2.67e-11	0.000	0	KIDA
C_2H_5	$O(^3P)$	-	CH_3CHO	H	-	1.33e-10	0.000	0	KIDA
C_2H_5	OH	-	CH_3CHO	H_2	-	1.00e-10	0.000	0	KIDA
C_2H_5	OH	-	C_2H_4	H_2O	-	4.00e-11	0.000	0	KIDA
C	OH	-	CO	H	-	1.15e-10	-0.340	0	KIDA
C	O_2	-	CO	$O(^3P)$	-	4.90e-11	-0.320	0	KIDA
CH	H	-	C	H_2	-	1.24e-10	0.260	0	KIDA
CH	$O(^3P)$	-	CO	H	-	6.60e-11	0.000	0	Baulch et al. (2005)
CH	H_2	-	$^3CH_2$	H	-	2.90e-10	0.000	1670	Baulch et al. (2005)
CH	O_2	-	CO	OH	-	8.30e-11	0.000	0	Lichtin et al. (1984)
CH	CO_2	-	HCO	CO	-	5.71e-12	0.000	345	Baulch et al. (1992)
$^3CH_2$	$O(^3P)$	-	H	HCO	-	3.40e-12	0.000	270	KIDA
$^3CH_2$	H	-	CH	H_2	-	2.00e-10	0.000	0	Baulch et al. (2005)
CH_2CO	H	-	CH_3	CO	-	6.89e-12	0.885	1430	Baulch et al. (2005)
CH_2CO	$O(^3P)$	-	H_2CO	CO	-	3.80e-12	0.000	680	Baulch et al. (1992)
CH_2CO	$^3CH_2$	-	C_2H_4	CO	-	2.90e-10	0.000	0	Canosa-mas et al. (1984)
CH_3CO	H	-	H_2	CH_2CO	-	1.92e-11	0.000	0	KIDA
CH_3CO	H	-	HCO	CH_3	-	1.03e-11	0.000	0	KIDA
CH_3CO	$O(^3P)$	-	CO_2	CH_3	-	2.63e-10	0.000	0	Baulch et al. (2005)
CH_3CO	$O(^3P)$	-	OH	CH_2CO	-	8.75e-11	0.000	0	Baulch et al. (2005)
CH_3CO	OH	-	H_2O	CH_2CO	-	2.01e-11	0.000	0	Tsang & Hampson (1986)
CH_3CO	CH_3	-	C_2H_6	CO	-	5.40e-11	0.000	0	Adachi et al. (1981)
CH_3CO	CH_3	-	CH_4	CH_2CO	-	1.00e-11	0.000	0	Hassinen et al. (1990)
CH_3CO	$^3CH_2$	-	CH_3	CH_2CO	-	3.00e-11	0.000	0	Tsang & Hampson (1986)
CH_3CO	C_2H	-	C_2H_2	CH_2CO	-	3.00e-11	0.000	0	Tsang & Hampson (1986)
CH_3CO	HCO	-	CO	CH_3CHO	-	1.50e-11	0.000	0	Tsang & Hampson (1986)
$^3CH_2$	$^3CH_2$	-	C_2H_2	H_2	-	2.00e-11	0.000	400	Baulch et al. (1992)
$^3CH_2$	$^3CH_2$	-	C_2H_2	H	H	1.80e-10	0.000	400	Baulch et al. (1992)
C_2H	$^1CH_2$	-	CH	C_2H_2	-	3.00e-11	0.000	0	Tsang & Hampson (1986)
C_2H	$^3CH_2$	-	CH	C_2H_2	-	3.00e-11	0.000	0	Tsang & Hampson (1986)
C_2H	O_2	-	CO	CO	H	3.00e-11	0.000	0	KIDA
C_2H	$O(^3P)$	-	CO	CH	-	2.41e-11	0.000	230	Devriendt & Peeters (1997)
C_2H	H_2	-	C_2H_2	H	-	1.95e-14	2.320	4	Baulch et al. (2005)
C_2H	CH_4	-	C_2H_2	CH_3	-	7.67e-12	0.940	328	Baulch et al. (2005)
C_2H	C_2H_5	-	C_2H_2	C_2H_4	-	3.00e-12	0.000	0	Tsang & Hampson (1986)
C_2	H_2	-	C_2H	H	-	1.77e-10	0.000	1469	Kasting (1990)
C_2	CH_4	-	C_2H	CH_3	-	5.05e-11	0.000	297	Kasting (1990)
C_2	$O(^3P)$	-	C	CO	-	5.00e-11	0.000	0	Kasting (1990)

Continued on next page

Table A2 – continued from previous page

R1	R2	R3	P1	P2	P3	A	α	β (K)	Source
C_2	O_2	-	CO	CO	-	1.50e-11	0.000	550	Kasting (1990)
$^3CH_2$	CH_3	-	C_2H_4	H	-	7.00e-11	0.000	0	Kasting (1990)
$^3CH_2$	C_2H_3	-	CH_3	C_2H_2	-	3.00e-11	0.000	0	Kasting (1990)
C_2H_3	H	-	C_2H_2	H_2	-	3.30e-11	0.000	0	Kasting (1990)
C_2H_3	H_2	-	C_2H_4	H	-	2.60e-13	0.000	2646	Kasting (1990)
C_2H_3	CH_4	-	C_2H_4	CH_3	-	2.40e-14	4.020	2754	Kasting (1990)
C_2H_3	C_2H_6	-	C_2H_4	C_2H_5	-	3.00e-13	0.000	5170	Kasting (1990)
C_2H_4	OH	-	H_2CO	CH_3	-	2.20e-12	0.000	-385	Kasting (1990)
C_2H_4	$O(^3P)$	-	HCO	CH_3	-	5.50e-12	0.000	565	Kasting (1990)
C_2H	C_2H_6	-	C_2H_2	C_2H_5	-	5.10e-11	0.000	76	KIDA
CH	CH_4	-	C_2H_4	H	-	6.66e-11	-0.400	0	Thiesemann et al. (1997)
$^3CH_2$	C_2H_5	-	CH_3	C_2H_4	-	3.00e-11	0.000	0	Tsang & Hampson (1986)
$O(^3P)$	C_2H_2	-	$^3CH_2$	CO	-	3.00e-11	0.000	1600	Burkholder et al. (2015)
C_2H_3	$O(^3P)$	-	CH_2CO	H	-	5.50e-11	0.000	0	Kasting (1990)
C_2H_3	OH	-	C_2H_2	H_2O	-	8.30e-12	0.000	0	Kasting (1990)
C_2H_3	CH_3	-	C_2H_2	CH_4	-	3.40e-11	0.000	0	Kasting (1990)
C_2H_3	C_2H_3	-	C_2H_4	C_2H_2	-	2.40e-11	0.000	0	Kasting (1990)
C_2H_3	C_2H_5	-	C_2H_4	C_2H_4	-	3.00e-12	0.000	0	Kasting (1990)
C_2H_5	C_2H_3	-	C_2H_6	C_2H_2	-	6.00e-12	0.000	0	Kasting (1990)
C_2H_5	C_2H_5	-	C_2H_6	C_2H_4	-	2.30e-12	0.000	0	Kasting (1990)
C_2H_2	OH	-	CH_2CO	H	-	1.00e-13	0.000	0	Kasting (1990)
C_2H_2OH	H	-	H_2O	C_2H_2	-	5.00e-11	0.000	0	Kasting (1990)
C_2H_2OH	H	-	H_2	CH_2CO	-	3.30e-11	0.000	2000	Kasting (1990)
C_2H_2OH	$O(^3P)$	-	OH	CH_2CO	-	3.30e-11	0.000	2000	Kasting (1990)
C_2H_2OH	OH	-	H_2O	CH_2CO	-	1.70e-11	0.000	1000	Kasting (1990)
C_2H_4OH	H	-	H_2O	C_2H_4	-	5.00e-11	0.000	0	Kasting (1990)
C_2H_4OH	H	-	H_2	CH_3CHO	-	3.30e-11	0.000	2000	Kasting (1990)
C_2H_4OH	$O(^3P)$	-	OH	CH_3CHO	-	3.30e-11	0.000	2000	Kasting (1990)
C_2H_4OH	OH	-	H_2O	CH_3CHO	-	1.70e-11	0.000	1000	Kasting (1990)
CH_3CHO	H	-	CH_3CO	H_2	-	2.80e-11	0.000	1540	Kasting (1990)
$O(^3P)$	CH_3CHO	-	CH_3CO	OH	-	1.80e-11	0.000	1100	Burkholder et al. (2015)
OH	CH_3CHO	-	CH_3CO	H_2O	-	4.63e-12	0.000	-350	Burkholder et al. (2015)
CH_3CHO	CH_3	-	CH_3CO	CH_4	-	2.80e-11	0.000	1540	Kasting (1990)
C_2H_5	CH_3	-	C_2H_4	CH_4	-	1.50e-12	0.000	0	Kasting (1990)
C_2H	HCO	-	CO	C_2H_2	-	1.00e-10	0.000	0	Tsang & Hampson (1986)
$O(^3P)$	CH_3	-	H_2CO	H	-	1.10e-10	0.000	0	Burkholder et al. (2019)
$O(^1D)$	CO_2	-	$O(^3P)$	CO_2	-	7.50e-11	0.000	-115	Burkholder et al. (2019)
CH_3O_2	O_3	-	CH_3O	O_2	O_2	2.90e-16	0.000	1000	Burkholder et al. (2015)
C_2H_4OH	O_2	-	CH_3CHO	HO_2	-	6.30e-14	0.000	550	Burkholder et al. (2015)
$O(^1D)$	O_3	-	O_2	O_2	-	1.20e-10	0.000	0	Burkholder et al. (2019)
$O(^1D)$	O_3	-	O_2	$O(^3P)$	$O(^3P)$	1.20e-10	0.000	0	Burkholder et al. (2019)
HS	CS	-	CS_2	H	-	1.50e-13	0.000	0	Burkholder et al. (2015)
CH_3	HNO	-	CH_4	NO	-	1.85e-11	0.600	176	Choi & Lin (2005)
N	O_2	-	NO	$O(^3P)$	-	3.30e-12	0.000	3150	Burkholder et al. (2019)
N	O_3	-	NO	O_2	-	0.00e+00	0.000	0	Burkholder et al. (2015)
N	OH	-	NO	H	-	5.00e-11	0.000	6	KIDA
N	NO	-	N_2	$O(^3P)$	-	2.10e-11	0.000	-100	Burkholder et al. (2019)
NO	O_3	-	NO_2	O_2	-	3.00e-12	0.000	1500	Burkholder et al. (2019)
HO_2	NO	-	NO_2	OH	-	3.44e-12	0.000	-260	Burkholder et al. (2019)
$O(^3P)$	NO_2	-	NO	O_2	-	5.30e-12	0.000	-200	Burkholder et al. (2019)
H	NO_2	-	OH	NO	-	1.35e-10	0.000	0	Burkholder et al. (2019)
HCO	NO	-	HNO	CO	-	1.35e-11	0.000	0	Dammeier et al. (2007)
HNO	hv	-	NO	H	-	1.70e-03	0.000	0	Dammeier et al. (2007)
H	HNO	-	H_2	NO	-	3.01e-11	0.000	500	Tsang & Herron (1991)
$O(^3P)$	HNO	-	OH	NO	-	3.80e-11	-0.080	0	KIDA
OH	HNO	-	H_2O	NO	-	8.00e-11	0.000	500	Tsang & Herron (1991)
OH	HNO_2	-	H_2O	NO_2	-	3.00e-12	0.000	-250	Burkholder et al. (2019)
C_2H_5	HNO	-	C_2H_6	NO	-	1.60e-12	0.000	1000	Zahnle (1986)

Table A2 – continued from previous page

R1	R2	R3	P1	P2	P3	A	α	β (K)	Source
HNO_3	OH	-	H_2O	NO_3	-	2.40e-14	0.000	-460	Burkholder et al. (2015)
N	HO_2	-	NO	OH	-	2.20e-11	0.000	0	Brune et al. (1983)
HO_2	NO_2	-	HNO_2	O_2	-	5.00e-16	0.000	0	Burkholder et al. (2015)
SO	O_2	-	SO_2	$O(^3P)$	-	1.60e-13	0.000	2280	Burkholder et al. (2015)
SO	HO_2	-	SO_2	OH	-	2.80e-11	0.000	0	Kasting (1990)
OH	SO	-	H	SO_2	-	2.70e-11	0.000	-335	Burkholder et al. (2015)
SO_3	H_2O	H_2O	H_2SO_4	H_2O	-	6.90e-14	1.000	-6540	Krasnopolsky (2012)
HSO_3	O_2	-	HO_2	SO_3	-	1.30e-12	0.000	330	Burkholder et al. (2015)
HSO_3	OH	-	H_2O	SO_3	-	1.00e-11	0.000	0	Kasting (1990)
HSO_3	H	-	H_2	SO_3	-	1.00e-11	0.000	0	Kasting (1990)
HSO_3	$O(^3P)$	-	OH	SO_3	-	1.00e-11	0.000	0	Kasting (1990)
OH	H_2S	-	HS	H_2O	-	6.10e-12	0.000	75	Burkholder et al. (2015)
H_2S	H	-	H_2	HS	-	3.66e-12	1.940	455	Peng et al. (1999)
$O(^3P)$	H_2S	-	OH	HS	-	9.20e-12	0.000	1800	Burkholder et al. (2015)
$O(^3P)$	HS	-	SO	H	-	7.00e-11	0.000	0	Burkholder et al. (2015)
HS	O_2	-	OH	SO	-	4.00e-19	0.000	0	Burkholder et al. (2015)
HS	HO_2	-	HSO	OH	-	1.00e-11	0.000	0	Stachnik & Molina (1987)
HS	HS	-	H_2S	S	-	1.50e-11	0.000	0	Schofield (1973); Tiee et al. (1981)
HS	HS	-	H_2	S_2	-	5.00e-14	0.000	0	Schofield (1973); Tiee et al. (1981)
HS	HCO	-	H_2S	CO	-	5.00e-11	0.000	0	Kasting (1990)
HS	H	-	H_2	S	-	2.00e-11	0.000	0	Tiee et al. (1981)
HS	S	-	H	S_2	-	5.00e-12	0.000	0	Nicholas et al. (1979)
S	O_2	-	SO	$O(^3P)$	-	1.60e-12	0.000	-100	Burkholder et al. (2015)
OH	S	-	H	SO	-	6.60e-11	0.000	0	Burkholder et al. (2015)
S	HCO	-	H	OCS	-	8.00e-11	0.000	0	Loison et al. (2012)
S	HCO	-	HS	CO	-	4.00e-11	0.000	0	Loison et al. (2012)
S	HO_2	-	HS	O_2	-	5.00e-12	0.000	0	Kasting (1990)
S	HO_2	-	SO	OH	-	5.00e-12	0.000	0	Kasting (1990)
S_2	$O(^3P)$	-	S	SO	-	1.66e-11	0.000	0	Singleton & Cvetanović (1988)
HS	H_2CO	-	H_2S	HCO	-	1.70e-11	0.000	800	Harman et al. (2015)
$^1SO_2$	M	-	$^3SO_2$	-	-	1.00e-12	0.000	0	Turco et al. (1982)
$^1SO_2$	M	-	SO_2	-	-	1.00e-11	0.000	0	Turco et al. (1982)
$^1SO_2$	$h\nu$	-	$^3SO_2$	-	-	1.50e+03	0.000	0	Turco et al. (1982)
$^1SO_2$	$h\nu$	-	SO_2	-	-	2.20e+04	0.000	0	Turco et al. (1982)
$^3SO_2$	O_2	-	SO_3	$O(^3P)$	-	1.00e-16	0.000	0	Turco et al. (1982)
$^1SO_2$	O_2	-	SO_3	$O(^3P)$	-	1.00e-16	0.000	0	Toon et al. (1987)
$^1SO_2$	SO_2	-	SO_3	SO	-	4.00e-12	0.000	0	Turco et al. (1982)
$^3SO_2$	M	-	SO_2	-	-	1.50e-13	0.000	0	Turco et al. (1982)
$^3SO_2$	$h\nu$	-	SO_2	-	-	1.13e+03	0.000	0	Turco et al. (1982)
$^3SO_2$	SO_2	-	SO_3	SO	-	7.00e-14	0.000	0	Turco et al. (1982)
SO	NO_2	-	SO_2	NO	-	1.40e-11	0.000	0	Burkholder et al. (2015)
SO	O_3	-	SO_2	O_2	-	3.40e-12	0.000	1100	Burkholder et al. (2015)
HO_2	SO_2	-	SO_3	OH	-	1.00e-18	0.000	0	Burkholder et al. (2015)
HS	O_3	-	HSO	O_2	-	9.00e-12	0.000	280	Burkholder et al. (2019)
HS	NO_2	-	HSO	NO	-	2.90e-11	0.000	-250	Burkholder et al. (2015)
S	O_3	-	SO	O_2	-	1.20e-11	0.000	0	Burkholder et al. (2015)
SO	SO	-	SO_2	S	-	2.00e-15	0.000	0	Chung et al. (1975); Martinez & Herron (1983)
SO_3	SO	-	SO_2	SO_2	-	2.00e-15	0.000	0	Chung et al. (1975)
S	CO_2	-	SO	CO	-	1.00e-20	0.000	0	Yung & Demore (1982)
HCO	SO	-	HSO	CO	-	5.20e-12	0.000	0	Assumed equal to HCO + $O_2 \rightarrow HO_2$ + CO
HSO	NO	-	HNO	SO	-	1.00e-15	0.000	0	Burkholder et al. (2019)
HSO	OH	-	H_2O	SO	-	4.80e-11	0.000	-250	Assumed same as OH + $HO_2 \rightarrow H_2O + O_2$
HSO	H	-	S	H_2O	-	1.60e-12	0.000	0	Assumed same as H + $HO_2 \rightarrow O(^3P) + H_2O$
HSO	H	-	HS	OH	-	7.20e-11	0.000	0	Assumed same as H + $HO_2 \rightarrow$ OH + OH
HSO	H	-	H_2	SO	-	6.90e-12	0.000	0	Assumed same as H + $HO_2 \rightarrow H_2 + O_2$
HSO	HS	-	H_2S	SO	-	3.00e-11	0.000	0	Zahnle et al. (2006)
HSO	$O(^3P)$	-	OH	SO	-	3.00e-11	0.000	-200	Assumed same as $O(^3P) + HO_2 \rightarrow$ OH + O_2
HSO	S	-	HS	SO	-	3.00e-11	0.000	0	Kasting (1990)

Table A2 – continued from previous page

R1	R2	R3	P1	P2	P3	A	α	β (K)	Source
H	OCS	-	CO	HS	-	9.07e-12	0.000	1940	Lee et al. (1977)
HS	CO	-	OCS	H	-	4.15e-14	0.000	7660	Kurbanov & Mamedov (1995)
O(^{1}D)	OCS	-	CO	SO	-	3.00e-10	0.000	0	Gauthier & Snelling (1975)
O(^{3}P)	OCS	-	CO	SO	-	2.10e-11	0.000	2200	Burkholder et al. (2015)
O(^{3}P)	OCS	-	S	CO_2	-	8.33e-11	0.000	5530	Singleton & Cvetanović (1988)
OCS	S	-	CO	S_2	-	1.90e-14	3.970	580	Lu et al. (2006)
OH	OCS	-	CO_2	HS	-	7.20e-14	0.000	1070	Burkholder et al. (2015)
HO_2	H_2S	-	H_2O	HSO	-	3.00e-15	0.000	0	Burkholder et al. (2015)
OCS_2	S	-	OCS	S_2	-	5.00e-12	0.000	0	Basco & Pearson (1967)
S_3	O(^{3}P)	-	S_2	SO	-	1.00e-16	0.000	0	Assumed equal to rate for S_2 + O(^{3}P)$\rightarrow$ S + SO
S_4	O(^{3}P)	-	S_3	SO	-	1.00e-16	0.000	0	Assumed equal to rate for S_2 + O(^{3}P)$\rightarrow$ S + SO
OCS_2	CO	-	OCS	OCS	-	3.00e-12	0.000	0	Zahnle et al. (2006)
CH_3O_2	NO	-	CH_3O	NO_2	-	2.80e-12	0.000	-300	Burkholder et al. (2015)
NO	CH_3O	-	HNO	H_2CO	-	2.30e-12	-0.700	0	IUPAC
CH_3O	NO_2	-	H_2CO	HNO_2	-	1.10e-11	0.000	1200	Burkholder et al. (2015)
O(^{3}P)	HNO_3	-	OH	NO_3	-	3.00e-17	0.000	0	Burkholder et al. (2015)
O(^{3}P)	N_2O_5	-	NO_2	NO_2	O_2	3.00e-16	0.000	0	Burkholder et al. (2015)
NO_2	NO_3	-	NO	NO_2	O_2	4.35e-14	0.000	1335	Burkholder et al. (2019)
NO_2	O_3	-	NO_3	O_2	-	1.20e-13	0.000	2450	Burkholder et al. (2019)
NO_3	NO_3	-	NO_2	NO_2	O_2	8.50e-13	0.000	2450	Burkholder et al. (2019)
O(^{3}P)	HO_2NO_2	-	OH	NO_2	O_2	7.80e-11	0.000	3400	Burkholder et al. (2015)
OH	HO_2NO_2	-	H_2O	NO_2	O_2	4.50e-13	0.000	-610	Burkholder et al. (2019)
O(^{3}P)	NO_3	-	O_2	NO_2	-	1.30e-11	0.000	0	Burkholder et al. (2019)
HO_2	NO_3	-	OH	NO_2	O_2	3.50e-12	0.000	0	Burkholder et al. (2019)
NO	NO_3	-	NO_2	NO_2	-	1.70e-11	0.000	-125	Burkholder et al. (2019)
OH	NO_3	-	HO_2	NO_2	-	2.00e-11	0.000	0	Burkholder et al. (2019)
N	NO_2	-	N_2O	O(^{3}P)	-	5.80e-12	0.000	-220	Burkholder et al. (2019)
O(^{1}D)	N_2O	-	N_2	O_2	-	4.64e-11	0.000	-20	Burkholder et al. (2019)
O(^{1}D)	N_2O	-	NO	NO	-	7.26e-11	0.000	-20	Burkholder et al. (2019)
CS	O_2	-	OCS	O(^{3}P)	-	2.75e-19	0.000	0	Burkholder et al. (2015)
CS	O_2	-	CO	SO	-	1.45e-20	0.000	0	Burkholder et al. (2015)
CS	O_3	-	OCS	O_2	-	3.00e-16	0.000	0	Burkholder et al. (2015)
CS_2	O(^{3}P)	-	CS	SO	-	2.88e-11	0.000	650	Burkholder et al. (2015)
CS_2	O(^{3}P)	-	CO	S_2	-	6.60e-13	0.000	650	Burkholder et al. (2015)
CS_2	O(^{3}P)	-	OCS	S	-	2.64e-12	0.000	650	Burkholder et al. (2015)
OH	CS_2	-	HS	OCS	-	2.00e-15	0.000	0	Burkholder et al. (2015)
CS_2^*	M	-	CS_2	M	-	2.50e-11	0.000	0	Wine et al. (1981); Toon et al. (1987)
CS_2^*	O_2	-	CS	SO_2	-	1.00e-12	0.000	0	Wine et al. (1981); Toon et al. (1987)
CS_2^*	CS_2	-	CS	CS	S_2	1.00e-12	0.000	0	Domagal-Goldman et al. (2011)
CS_2	SO	-	OCS	S_2	-	1.60e-13	0.000	2280	Assumed same as SO + O_2
O(^{3}P)	CS	-	CO	S	-	2.70e-10	0.000	760	Burkholder et al. (2015)
H	HCS	-	H_2	CS	-	1.83e-10	0.000	0	Assumed same as H + HCO $\rightarrow$ H_2 + CO
S	HCS	-	H	CS_2	-	5.00e-11	0.000	0	Assumed same as O(^{3}P)+ HCO $\rightarrow$ H + O_2
S	HCS	-	HS	CS	-	5.00e-11	0.000	0	Assumed same as O(^{3}P)+ HCO $\rightarrow$ OH + CO
$^1CH_2$	S_2	-	H	CS	HS	2.05e-11	0.000	750	Assumed same as $^1CH_2$ + O_2 $\rightarrow$ H + CO + OH
$^1CH_2$	S_2	-	H_2	CS_2	-	2.05e-11	0.000	750	Assumed same as $^1CH_2$ + O_2 $\rightarrow$ H_2 + CO_2
$^3CH_2$	S_2	-	HCS	HS	-	4.10e-11	0.000	750	Assumed same as $^3CH_2$ + O_2 $\rightarrow$ HCO + OH
CH_3	HCS	-	CH_4	CS	-	9.30e-11	0.000	0	Assumed same as CH3 + HCO $\rightarrow$ CH4 + CO
$^3CH_2$	S	-	CS	H_2	-	9.86e-11	0.000	270	Assumed same as $^3CH_2$ + O(^{3}P)$\rightarrow$ CO + H2
$^3CH_2$	S	-	H	HCS	-	3.40e-12	0.000	270	Assumed same as $^3CH_2$ + O(^{3}P)$\rightarrow$ H + HCO
$^3CH_2$	S	-	CS	H	H	2.38e-10	0.000	270	Assumed same as $^3CH_2$ + O(^{3}P)$\rightarrow$ CO + H + H
HS	HCS	-	H_2S	CS	-	5.00e-11	0.000	0	Assumed same as HS + HCO $\rightarrow$ H_2S + CO
C	HS	-	CS	H	-	2.00e-10	0.000	0	KIDA
C	S_2	-	CS	S	-	4.90e-11	-0.320	0	Assumed same as C + O_2 $\rightarrow$ CO + O(^{3}P)
CH	S	-	CS	H	-	6.60e-11	0.000	0	Assumed same as CH + O(^{3}P)$\rightarrow$ CO + H
CH	S_2	-	CS	HS	-	8.30e-11	0.000	0	Assumed same as CH + O_2 $\rightarrow$ CO + OH
CH	CS_2	-	HCS	CS	-	3.49e-10	0.000	40	Zabarnick et al. (1989)

Continued on next page

Table A2 – continued from previous page

R1	R2	R3	P1	P2	P3	A	α	β (K)	Source
OCS	CH	-	H	CO	CS	1.99e-10	0.000	-190	Zabarnick et al. (1989)
C_2	S	-	C	CS	-	5.00e-11	0.000	0	Kasting (1990)
C_2	S_2	-	CS	CS	-	1.50e-11	0.000	550	Kasting (1990)
$O(^1D)$	SO_2	-	$O(^3P)$	SO_2	-	5.28e-11	0.000	0	Burkholder et al. (2019)
$O(^1D)$	SO_2	-	SO	O_2	-	1.67e-10	0.000	0	Burkholder et al. (2019)
HS	H_2O_2	-	H_2S	HO_2	-	5.00e-15	0.000	0	Burkholder et al. (2019)
HSO	O_2	-	HS	O_3	-	2.00e-17	0.000	0	Burkholder et al. (2019)
HSO	O_3	-	HS	O_2	O_2	1.00e-13	0.000	0	Burkholder et al. (2019)
CS	NO_2	-	OCS	NO	-	7.60e-17	0.000	0	Burkholder et al. (2015)
N_2O_5	H_2O	-	HNO_3	HNO_3	-	2.00e-21	0.000	0	Burkholder et al. (2019)
SO	HO_2	-	HSO	O_2	-	2.80e-11	0.000	0	Harman et al. (2015)
HSO	NO_2	-	HNO	SO	-	1.00e-15	0.000	0	Harman et al. (2015)

Table A3: Termolecular reactions used in this network. Reactions sourced from the Kinetic Database for Astrochemistry (KIDA) are from https://kida.astrochem-tools.org/ and those sourced from the International Union of Pure and Applied Chemistry (IUPAC) are obtained from https://iupac-aeris.ipsl.fr/. The horizontal line within the table shows the cutoff for the CHO network.

R1	R2	P1	P2	A_1	α_1	β_1 (K)	A_2	α_2	β_2 (K)	F_c	Source
H	O_2	HO_2	-	5.30e-32	-1.800	0	9.50e-11	0.400	0	0.600	Burkholder et al. (2019)
HO_2	HO_2	H_2O_2	O_2	2.10e-33	0.000	-920	1.00e-10	0.000	0	0.600	Burkholder et al. (2019)
$O(3P)$	$O(3P)$	O_2	-	9.46e-34	0.000	-485	1.00e-10	0.000	0	0.600	Campbell & Gray (1973)
$O(3P)$	O_2	O_3	-	6.10e-34	-2.400	0	1.00e-10	0.000	0	0.600	Burkholder et al. (2019)
CO	$O(3P)$	CO_2	-	6.51e-33	0.000	2188	1.00e-10	0.000	0	0.600	Slanger et al. (1972)
H	CO	HCO	-	5.29e-34	0.000	373	1.00e-10	0.000	0	0.600	KIDA
H	H	H_2	-	8.85e-33	-0.600	0	1.00e-10	0.000	0	0.600	Baulch et al. (1992)
H	OH	H_2O	-	6.78e-31	-2.000	0	1.00e-10	0.000	0	0.600	KIDA
OH	OH	H_2O_2	-	6.90e-31	-1.000	0	2.60e-11	0.000	0	0.600	Burkholder et al. (2019)
CH_3	CH_3	C_2H_6	-	1.13e-25	-3.750	494	7.42e-11	-0.690	88	0.600	KIDA
CH_3	H	CH_4	-	2.63e-28	-2.980	635	3.50e-10	0.000	0	1.000	KIDA
CH_3	O_2	CH_3O_2	-	4.00e-31	-3.600	0	1.20e-12	1.100	0	0.600	Burkholder et al. (2015)
C_2H_5	H	C_2H_6	-	6.11e-28	-2.000	1040	1.66e-10	0.000	0	1.000	KIDA
C	H_2	$^3CH_2$	-	7.00e-32	0.000	0	2.06e-11	0.000	55	1.000	KIDA
CH	H_2	CH_3	-	5.11e-30	-1.600	0	2.00e-11	0.150	0	0.798	Baulch et al. (2005)
$^3CH_2$	H	CH_3	-	3.10e-30	0.000	-457	1.50e-10	0.000	0	0.600	Gladstone et al. (1996)
$^3CH_2$	CO	CH2CO	-	1.00e-28	0.000	0	1.00e-15	0.000	0	0.600	Yung et al. (1984)
CH_3	CO	CH_3CO	-	5.90e-36	0.000	0	1.24e-13	1.050	2850	0.600	Baulch et al. (2005)
C_2H	H	C_2H_2	-	2.64e-26	-3.100	721	3.00e-10	0.000	0	1.000	Tsang & Hampson (1986)
C_2H_2	H	C_2H_3	-	2.60e-31	0.000	0	3.80e-11	0.000	1374	0.600	Kasting (1990)
C_2H_4	H	C_2H_5	-	2.15e-29	0.000	349	4.95e-11	0.000	1051	0.600	Kasting (1990)
OH	C_2H_2	C_2H_2OH	-	5.50e-30	0.000	0	8.30e-13	2.000	0	0.600	Burkholder et al. (2015)
OH	C_2H_4	C_2H_4OH	-	1.10e-28	-3.500	0	8.40e-12	-1.750	0	0.600	Burkholder et al. (2015)
H	NO	HNO	-	1.34e-31	-1.320	370	2.44e-10	-0.410	0	0.600	Tsang & Herron (1991)
N	N	N_2	-	4.10e-34	0.000	0	1.00e-10	0.000	0	0.600	KIDA
$O(3P)$	NO	NO_2	-	9.10e-32	-1.500	0	3.00e-11	0.000	0	0.600	Burkholder et al. (2019)
OH	NO	HNO_2	-	7.10e-31	-2.600	0	3.60e-11	-0.100	0	0.600	Burkholder et al. (2019)
OH	NO_2	HNO_3	-	1.80e-30	-3.000	0	2.80e-11	0.000	0	0.600	Burkholder et al. (2019)
HNO_3	OH	H_2O	NO_3	6.50e-34	0.000	-1335	2.70e-17	0.000	-2199	1.000	Burkholder et al. (2015)
SO	$O(3P)$	SO_2	-	5.10e-31	0.000	0	5.31e-11	0.000	0	0.600	Singleton & Cvetanović (1988)
OH	SO_2	HSO3	-	3.30e-31	-4.300	0	1.60e-12	0.000	0	0.600	Burkholder et al. (2015)
$O(3P)$	SO_2	SO_3	-	1.80e-33	2.000	0	4.20e-14	1.800	0	0.600	Burkholder et al. (2015)
S	S	S_2	-	1.00e-33	0.000	-206	2.26e-14	0.000	-415	0.600	Du et al. (2008); Babikov et al. (2017)
S	S_2	S_3	-	1.65e-33	0.000	-144	1.38e-14	0.000	-450	0.600	Du et al. (2011)
S_2	S_2	S_4	-	2.50e-30	0.000	0	5.00e-11	0.000	0	0.600	Langford & Oldershaw (1972)
S	S_3	S_4	-	1.65e-33	0.000	-144	1.38e-14	0.000	-450	0.600	Assumed equal to S +$S_2 \rightarrow S_3$
S_4	S_4	S_8	-	2.50e-30	0.000	0	5.00e-11	0.000	0	0.600	Assumed equal to $S_2 + S_2 \rightarrow S_4$
H	SO	HSO	-	4.40e-32	-1.300	0	7.50e-11	0.200	0	0.600	Assumed equal to H + O_2 + M $\rightarrow$ HO_2 + M
CO	S	OCS	-	6.51e-33	0.000	2188	1.00e-10	0.000	0	0.600	Assumed equal to $O(3P)$+ CO + M $\rightarrow CO_2$

Continued on next page

Table A3 – continued from previous page

R1	R2	P1	P2	A_1	α_1	β_1 (K)	A_2	α_2	β_2 (K)	F_c	Source
OCS	S	OCS_2	-	9.72e-25	-6.980	6046	3.50e-11	-8.220	4206	0.600	Lu et al. (2006)
NO_2	NO_3	N_2O_5	-	2.40e-30	-3.000	0	1.60e-12	0.100	0	0.600	Burkholder et al. (2019)
N_2O_5	-	NO_3	NO_2	1.30e-03	-3.500	11000	9.70e+14	0.100	11080	0.350	IUPAC
HO_2	NO_2	HO_2NO_2	-	1.90e-31	-3.400	0	4.00e-12	-0.300	0	0.600	Burkholder et al. (2019)
HO_2NO_2	-	HO_2	NO_2	4.10e-05	0.000	10650	6.00e+15	0.000	11170	0.400	IUPAC
O(3P)	NO_2	NO_3	-	3.40e-31	-1.600	0	2.30e-11	-0.200	0	0.600	Burkholder et al. (2019)
O(1D)	N_2	N_2O	-	2.80e-36	-0.900	0	1.00e-10	0.000	0	0.600	Burkholder et al. (2019)
CS2	S	CS	S_2	7.40e-31	0.000	0	2.20e-12	0.000	0	0.600	Gao & Marshall (2011)
H	CS	HCS	-	5.29e-34	0.000	373	1.00e-10	0.000	0	0.600	Assumed same as H + CO → HCO